LhARA-Gov-PMB-2024-08 Final
1272-pa1-pm-rpt-0009-1.0-18-month-design-review-report

July 21, 2024

Ion Therapy Research Facility / LhARA: eighteen month progress report

C. Baker [1], J. Bamber [2], W. Bertsche [3,4], R. Bingham [5,6], E. Boella [8,4], M. Charlton [1], B. Cox [9], T. Dascalu [8], N.P. Dover [15], S.J. Eriksson [1], A.Giacca [12], A. Goulden [7,4], R.J. Gray [5,4], C. Hill [7], P.R. Hobson [12], C.A. Isaac [1], M. Johnson [7,4], K. Kirkby [13,3,4], N. Kumar [14,4], K.R. Long [10,15], P. McKenna [5,4], R. Mclauchlan [16], M.Maxouti [10,15], H. Owen [7,4], C.A.J. Palmer [17], J.L. Parsons [16], J. Pasternak [10,15], M. Patel [14,4], T. Price [18], C. Pugh [7], P. Ruksasakchai [1], F. Thesni M. P. [14,4], W. Shields [19], D.P. van der Werf [1], A. Vikhoreva [7], C. Welsch [14,4], C. Whyte [5,4]

For the collaboration

1. *Department of Physics, Faculty of Science and Engineering, Swansea University, Singleton Park, Swansea, SA2 8PP*
2. *Institute of Cancer Research, UK*
3. *Department of Physics and Astronomy, The University of Manchester, Oxford Rd, Manchester, M13 9PL, UK*
4. *Cockcroft Institute, Sci-Tech Daresbury, Daresbury, Warrington, WA4 4AD, UK*
5. *Department of Physics, SUPA, University of Strathclyde, 16 Richmond Street, Glasgow, G1 1XQ, UK*
6. *UKRI-STFC Rutherford Appleton Laboratory, Didcot, OX11 0QX, UK*
7. *UKRI-STFC Daresbury Laboratory, Sci-Tech Daresbury, Daresbury, Warrington, WA4 4AD, UK*
8. *Lancaster University, UK*
9. *Department of Medical Physics and Biomedical Engineering, Faculty of Engineering Science, University College London, Gower Street, London, WC1E 6BT, UK*
10. *Imperial College NHS Healthcare Trust, The Bays, South Wharf Road, St Mary's Hospital, London W2 1NY, UK*
11. *Oxford Institute of Radiation Oncology, Department of Oncology, University of Oxford, Old Road Campus Research Building, Roosevelt Drive, Oxford, OX3 7DQ, UK*
12. *Queen Mary University of London, Mile End Road, London E1 4NS, UK*
13. *Division of Cancer Sciences, Faculty of Biology, Medicine and Health, The University of Manchester, The Christie Proton Therapy Centre, The Christie NHS Foundation Trust, Wilmslow Rd, Manchester M20 4BX*
14. *Department of Physics, University of Liverpool, Liverpool L3 9TA, UK*
15. *The John Adams Institute for Accelerator Science, Imperial College London, Exhibition Road, London, SW7 2AZ, UK*
16. *Institute of Cancer and Genomic Sciences, University of Birmingham, Edgbaston, Birmingham, B15 2TT, UK*
17. *Queens University Belfast, University Road, Belfast, BT7 1NN, Northern Ireland, UK*
18. *School of Physics and Astronomy, University of Birmingham, Edgbaston, Birmingham, B15 2TT, UK*
19. *Royal Holloway, University of London, Egham, Surrey TW20 0EX*

Contents

Introduction

The UKRI Infrastructure Fund is investing £2M over two years (October 2022 to September 2024) in a Preliminary Activity (PA1) to deliver the conceptual design report (CDR) for the Ion Therapy Research Facility. Served by LhARA, the Laser-hybrid Accelerator for Radiobiological Applications, the ITRF will be the world's first facility dedicated to the study of the biological impact of ions from protons through carbon created by a laser-driven source. The facility will be capable of delivering ultra-high dose-rates in both conventional and magnetically-focused mini-beam formats, for both *in-vivo* and *in-vitro* experiments. This report summarises the progress made in PA1 over the first 18 months of the project.

The laser-driven source may be triggered to deliver dose "on demand" or in arbitrary temporal patterns, with a minimum bunch separation determined by the repetition rate of the laser, for which the baseline specification is 10 Hz. The baseline capture energy is significantly larger ($\sim$ 200 times for protons) than that provided by typical ion-discharge sources in use today. This suppresses the effect of the mutual repulsion of the ions allowing a significant increase in the instantaneous dose rate that can be delivered. The laser-hybrid approach, therefore, will allow the ITRF to provide a step-change in the beams available for radiobiological investigation.

The ITRF will be a flagship facility, guided by the needs of the clinical oncology community and designed for radiobiological and clinical researchers. The technologies demonstrated in LhARA have the potential to transform the clinical practice of particle beam therapy by providing a compact, fully automated facility capable of delivering a variety of ions in a broad range of time structures, spectral distributions, and spatial configurations at instantaneous dose rates up to and potentially significantly beyond the current ultra-high dose-rate "FLASH" regime.

Highlights of progress

The significant progress made in all aspects of the Preliminary Activity is reported in section 1. Particular highlights of progress over the past six month include:

- Experiments at the SCAPA facility at the University of Strathclyde have demonstrated the capability to run at a repetition rate of 1 Hz for extended periods. This is an important step on the way to the LhARA baseline repetition rate of 10 Hz. Work to develop the laser and target systems necessary to reach the LhARA baseline repetition rate of 10 Hz is underway at Strathclyde and Imperial.
- The engineering design of the Stage 1 beam line has progressed to include vacuum, control, safety and diagnostic systems. In addition, the design of the fixed-field accelerator (FFA) ring that boosts the energy in Stage 2 now includes concepts for the magnetic alloy cavities and a more complete design for the bending magnets. Space conflicts identified in the integration of these components in the design are being addressed.
- Measurement of the properties of electron plasma trapping and confinement have restarted at the University of Swansea. These measurements include spinning the plasma using the "rotating wall" technique. A significant increase in plama density and stablility have been achieved.
- The construction of the "SmartPhantom", that will be used to prove the principle of the ion-acoustic dose-profile measurement technique is complete. Discussions with colleagues at the Ludwig Maximilian Universität (LMU) in Munich regarding a collaborative experiment on the LION beam line at the LMU CALA facility at the Ludwigs Maximillian Universität, Munich are progressing well. Dates in the late summer or autumn'24 are under discussion.

Looking beyond the present Preliminary Activity, the project team have made good progress on the design of the permanent-quadrupole magnet beam that will be installed on SCAPA to serve an initial series of radiobiology experiments. Beam time for a pilot run has been reserved on SCAPA in December 2024. It is hoped that this will lead to a first exposure to test the concepts for the biological proof-of-principle experiment (PoPLaR)

in January 2025. This activity, in combination with the planned exposure of the SmartPhantom on the LION beam line at LMU in the autumn of 2024, will be significant in the development of the future ITRF/LhARA programme.

Development of the ITRF/LhARA programme beyond September 2024

The 12-month progress report [1] explained that the project team had been encouraged to submit a proposal for a second Preliminary Activity (PA2). The PA2 proposal defined a 4-year programme to be delivered over 5 financial years that would build on the CDR delivered in PA1 and which would deliver:

- Technical Design Reports for the staged implementation of the facility;
- A site study leading to site selection and building implementation plan; and
- A proof-of-principle demonstrator system at an existing pulsed-laser facility.

This proposal, submitted in June 2023, 9 months into the first preliminary activity, was ranked "High priority" by the Visions Team but was not selected for submission by STFC. In view of the broad support for the ITRF/LhARA initiative, its high impact potential, and its potential to deliver a step change in capability, £2M has been secured from UKRI to support a 2-year bridging activity to allow a proposal for the full infrastructure to be developed.

0 Work package 0: Project management

0.1 Project Organisation

The baseline specification for LhARA serving the ITRF is that the beam will be delivered at a repetition rate of 10 Hz [1–4]. Two options for the acceleration of the beams after Stage 1 (the laser-driven source and plasma lens beam capture system) have been considered. The baseline option being a fixed-field accelerator (FFA) and the alternative being a rapid-cycling synchrotron. The design of a rapid-cycling synchrotron (RCS) capable of accelerating the beam delivered by LhARA Stage 1 at a repetition rate of 1 Hz was presented in the 12-month progress report [1]. The baseline specification of a repetition rate of 10 Hz can be accommodated in the baseline FFA. Therefore, the FFA option has been confirmed as the baseline for acceleration in Stage 2. The RCS design is retained as a backup.

The confirmation of the baseline accelerator technology has allowed steps to be taken over the reporting period to complete the integration of the ITRF and LhARA organisations. To this end, the ITRF Project Manager and ITRF Project Scientist (Andy Goulden and Hywel Owen respectively) accepted invitations to join the LhARA executive board (LhARA-EB). The first meeting of the expanded LhARA-EB took place on the 6^{th} March 2024 and included invitations to the ITRF Project sponsor (M. Noro) and ASTeC Director (J. Clarke). At this meeting an outline structure and cost envelope for the future Bridging Funds application were developed. The future project was re-structured to reflect the new priorities:

- Work Package A: An experimental radiobiological program;
- Work Package B: Risk reduction activity for the future ITRF/LhARA facility; and
- Work Package C: Project management, outreach and engagement.

Within the new structure, the LhARA work packages continue under their current leadership and effort from the national labs is integrated within the work packages. Iteration of the project objectives and deliverables with the work-package managers resulted in a revised funding distribution which fits within the bridging period funding envelope. The per-annum funding remains problematic.

At short notice a formal application for bridging funds was completed and submitted on 22^{nd} April 2024 to the STFC Executive Board for consideration on 23^{rd} April 2024. The application was transmitted to the UKRI Infrastructure Advisory Committee. Notice of the award of £2M for a 2-year bridging period starting on the 1^{st}

October 2024 was given to the Project Sponsor on the 17th June 2024. A document detailing the allocations by work package and the bridging-period milestones will be completed in due course.

1 Work package 1: LhARA

The LhARA work packages are:

- WP1.1: Project Management;
- WP1.2: Laser driven ion source;
- WP1.3: Proton and ion capture;
- WP1.4: Real-time dose-deposition profiling;
- WP1.5: Novel, automated end-station development; and
- WP1.6: Facility design and integration.

1.1 Work package 1.1: Project Management

The LhARA project is managed through bi-weekly meetings of the Project Management Board (PMB) [5]. The PMB is attended by all Work Package Managers and is chaired by the LhARA Project Manager. Individual Work Packages [6–10] hold weekly or bi-weekly meetings to which the PMB and LhARA Executive Board [11] have standing invitations; attendance at these meetings allows the management team to engage directly with the R&D programme, monitor progress, and stay abreast of developments.

The LhARA PMB provides monthly reports to the ITRF project manager. These reports include spend to date, highlights of progress and raise issues as they arise. The reports also include a forward look to the next months of planned activity. The monthly reports to the ITRF are condensed from monthly reports provided by the work package managers to the PMB.

Overview of progress

Progress to date has largely been as planned and no un-anticipated risks have been identified. The risks related to the recruitment of new staff and staff retention in work packages 1.2, 1.3 and 1.5 identified in the previous report continue to be relevant. In WP1.3 the planned experimental campaign has been significantly delayed but is now progressing well. Milestone 3.1 was moved back to April 24 and the simulation component will be reduced. Milestones 3.2 and 3.3 can still be delivered within the PA1 timeframe, but the level of detail will be reduced. A no-cost extension has been granted to Swansea, this will ensure the planned effort is delivered to the project as the results become available.

WP1.2 experienced similar delays to new staff recruitment for the modelling effort. This has resulted in a full year's delay in securing staff in post. The new PDRA staff member is being supported principally by the rest of the WP2 staff who have also been able to source some limited additional simulation resource from their own groups. These simulations are sophisticated and the learning curve for the new PDRA was steep. However, work is now progressing well. The impact has been successfully confined to the simulation aspects of Milestone 2.1. LhARA management allowed WP1.2 to slip the simulation part of Milestone 2.1 to May 2024 to exploit fully the staffing resources that are now available. This report was completed on the 10th June 2024. Milestone 2.1 is not a pre-cursor for following work and the only requirement is that the results are available in good time for the final report in September 2024, there is therefore no reason to hold the original milestone date. Experimental work in WP1.2 had been progressing well with a successful series of continuous operation runs accumulating a large number of shots at lower proton energies. As the team pushed on with work using configurations capable of producing higher proton energies, a saturation in peak proton energy became apparent. Investigation of the reasons for the saturation have ruled out many possibilities and recently

identified an early pre-pulse as the responsible factor. This type of problem is relatively familiar to facilities investigating laser-solid interactions where pre-pulse energy can critically affect operation (in contrast to laser-gas interactions which are more tolerant). Tried and tested solutions such as "wedged" optics are known to offer a solution if they can be employed in the correct location, the problem therefore reduces to finding the offending optic(s), which can be non-trivial. The SCAPA facility team recently resolved the pre-pulse issue with the result that subsequent testing has shown improved proton energies with a cut off energy of 15 MeV. This satisfies the original WP2 objectives for the development of laser-driven proton source.

Staff recruitment issues in WP5 remain as previously reported, no further problems have been identified.

WP1.6 has produced two milestone deliverables this reporting period as well as contributing to the larger 18 month report deliverable. The LhARA Stage 1 beamline has now moved to a 7 plasma-lens design. The new configuration offers improved flexibility to deliver both the required range of beam sizes at the endstation and a beam suitable for injection into the FFA. The dose calculation has been cross checked against independent estimations. The variations were small and an update of the LhARA baseline has been prepared for discussion prior to its adoption as the new baseline.

Development of baseline configuration and radiation-biology programme

A first update of the LhARA FFA design has been developed and the project team is working towards a formal revision of the baseline. The revision of the baseline will follow the change-control procedure defined in [12]. The status of the work is is reported in section 1.6. Considerable work has been done to translate the magnetic field maps into engineering models and to adopt them into the CAD model of the facility. In this regard, co-operation between the LhARA and FETS FFA teams has been particularly fruitful. Engineering staff at Daresbury worked with the FETS FFA team to move their magnet model into CAD and to start to engineer the required ancillary structures such as coil-cooling manifolds and power feeds. In this work power-consumption issues were identified and mitigation techniques developed which have been applied to the LhARA FFA magnet design. The LhARA FFA magnet design is now in a comparatively advanced state with acceptable predicted power consumption. There remains the issue of trim-coil manufacture, as each magnet requires a large number of unique windings which must nest together. This will be a challenge in terms of accuracy as well as cost and represents one of the more important conclusions related to the FFA design to date. Outline designs for some additional FFA components including the FFA RF cavities and injection/extraction lines have been made. These designs have uniformly illuminated space conflicts and integration problems which the team has worked to resolve.

The LhARA collaboration has started the development of a proof-of-principal ("PoPLaR") radiobiology experiment. The objective is to leverage the existing infrastructure at SCAPA (installed to support VHEE radiobiology, but never commissioned) to start generating radiobiology results as soon as possible. The configuration will use compact, high-field permanent magnet quadrupoles to capture and transport a proton beam from the existing SCAPA system. A compact beam-transport system, designed using a new bespoke code, transporting a beam drawn from a representative initial proton distribution will deliver protons filtered through an energy selecting aperture to test cells held in a fixture developed for LhARA test exposures at the Birmingham cyclotron, The primary focus of this work will be to:

- Develop beamline and bespoke facilities at SCAPA for radiobiology experimentation;
- Publish preliminary results from cell survival/DNA damage experiments with laser-accelerated protons at SCAPA;
- Measure the relative biological effectiveness (RBE) of laser-accelerated protons using established cell lines for comparison with the RBE measured at conventional cyclotron-driven facilities; and
- Assess DNA damage repair kinetics and immunopeptidomic analysis of laser-accelerated protons.

Highlights of progress

Progress in the individual work packages is covered in the sections which follow and will not be repeated here. Highlights of the programme to date include:

- Three peer-group-consultation meetings have taken place (see [13, 14]). Each was well attended and engaged participants from the UK and overseas. A fourth meeting is planned for later in 2024 in Birmingham.
- Design and engineering of the LhARA stage 1 design. The LhARA Stage 1 design is now in an advanced state with all control and diagnostic systems accommodated within the full engineering model,
- Design and engineering of the LhARA FFA including cavity and magnet designs. LhARA has completed a new FFA lattice design. Integration engineering of the FFA has identified several space conflicts between the new component designs and the team are working steadily through these issues. The magnet design is advancing steadily. Several potential areas of concern have been mitigated through a better understanding of the optimisation process used in the magnet design.
- The ion-acoustic dose-profile measurement proof-of-principle experiment is under construction. The "SmartPhantom" will use liquid-scintillator to calibrate the acoustic signal generated by the passage of the ion beam. A first exposure to demonstrate the optical signal capture will take place in June 2024 at the Birmingham synchrotron. Discussions with LMU on a collaborative experiment on the LION beam line at the CALA facility at the Ludwigs Maximillian Universität, Munich are progressing well with potential dates in late summer or autumn'24 under discussion.
- The first period of continuous high repetition rate running has been completed at SCAPA. Analysis of the results shows excellent reproducibility.
- Milestone M3. Plasma experiments with existing Swansea experimental set-up.
- Milestone M6. Preliminary design of LhARA MA RF cavity, FFA magnet, diagnostic system, control and feedback systems complete.
- Milestone M7. Preliminary design study of LhARA Building concept design, bulk shielding assessment, mechanical systems integration support concepts, vacuum concepts, power consumption and cooling requirements complete.
- Milestone M10. Geant4 simulations of beam energy deposition profile.
- Milestone M11. Refined ITRF specifications and designs (18 month design review). This document.

LhARA Collaboration meeting #5 (CM5) took place on the 25^{th} and 26^{th} April at Imperial College London and the Institute of Cancer Research [15]. The meeting was split over two days to accommodate the expanded content and included the ITRF PA1 18-month progress review. Provision was made to assess, comment on and approve the recently completed milestone reports. ¡

1.2 Work package 1.2: Laser driven ion source

1.2.1 Overview of recent progress in WP1.2

WP1.2 is focused on the development and testing of the technology required for the LhARA laser-driven ion source. WP1.2 has successfully developed an active collaboration between all the major laser driven ion source groups in the UK, including the University of Strathclyde, Queen's University Belfast, Lancaster University, Imperial College London, and the Central Laser Facility. The collaboration is working effectively, with regular meetings and cross institute collaborative projects. The funding from the ITRF has enabled increased staff effort at the partner institutes, and is allowing us to make clear progress towards our objectives.

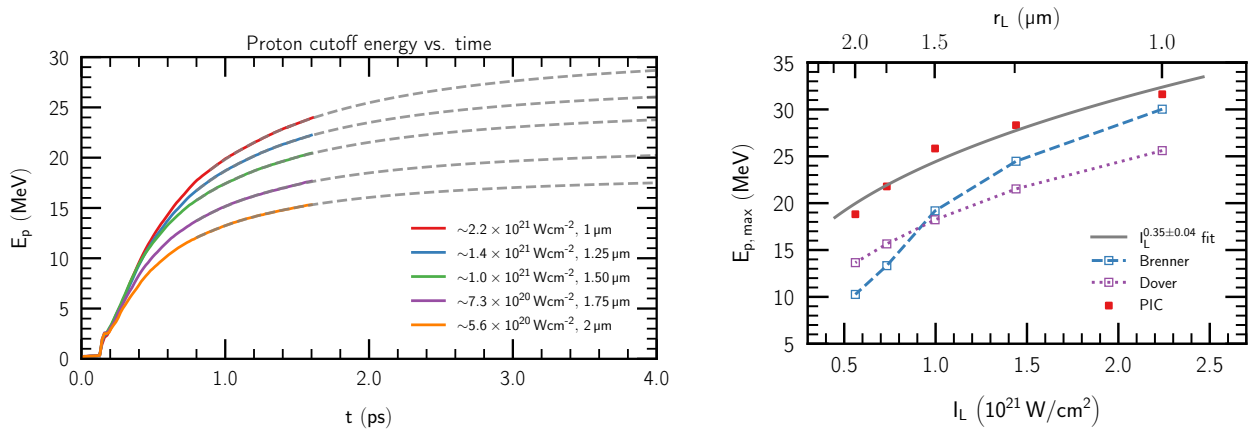

Figure 1: Evolution of the proton cut-off energy for different laser spot sizes at the focal plane (right panel). A model was fitted to the data from simulations to infer the maximum proton energies at later times. Proton cut-off energy at saturation vs laser intensity (left panel). The laser intensity was varied by changing the laser focal spot size at constant pulse energy. A power law fit is applied to the data from simulations. The predictions of two models of TNSA are also shown.

1.2.2 Update on Simulations

The programme of high-fidelity simulations have continued. Additional scans over laser and target parameters have been made to explore the impact of the angle of incidence of the laser and the focal spot-size on the effectiveness of proton acceleration via target-normal sheath acceleration (TNSA). Furthermore, we implemented a more realistic density profile for the pre-plasma in the Particle-In-Cell (PIC) simulations based on separate hydrodynamic simulations and a preliminary measurement of the laser contrast from SCAPA. Finally, we carried out an optimisation procedure to find the pre-plasma density profile that maximises the energy transfer from the laser to hot electrons, thus pushing the proton cut-off energy to higher values.

We have conducted realistic two- and three-dimensional PIC simulations exploring the interaction of the SCAPA Ti:sapphire laser (laser wavelength $\lambda_0 = 800\,\mathrm{nm}$) with $6\,\mu\mathrm{m}$ thick aluminium foils. We performed simulations considering a laser intensity of $9.97 \times 10^{20}\,\mathrm{W/cm^2}$ for normalised vector potential $a_0 = 21.60$. The p-polarised pulses were focused on the target to a spot size, w_0, of $1.5\,\mu\mathrm{m}$ and had a FWHM pulse duration of 25 fs. The target was modelled as a pre-formed plasma composed of Al^{3+} ions and electrons with density $70\,n_c \sim 10^{23}\,\mathrm{cm^{-3}}$ (here n_c is the critical density corresponding to the laser frequency). On the back of the target, a thin layer of H^+ ions was inserted to mimic contaminants naturally present on the back surface of solid targets.

We carried out a first set of 3-D PIC simulations considering values of the focal spot size, w_0, in the range 1.0–2.0 µm corresponding to laser intensities in the range 5.61×10^{20}–$2.24 \times 10^{21}\,\mathrm{W/cm^2}$ (normalised vector potential, a_0, in the range 16.2–32.4). The $6\,\mu$m-thick aluminium target was considered to have a pre-plasma on the front surface modelled as a hyperbolic tangent density profile with scale-length $L_g = 0.5\,\mu\mathrm{m}$. The proton cut-off energies resulting from the scan of the spot-size are shown in figure 1. In the presence of a pre-plasma with sub-micrometer scale-length, intensities higher than $\sim 7 \times 10^{20}\,\mathrm{W/cm^2}$ would be required to accelerate protons to energies of more than 15 MeV and meet the LhARA requirements. A smaller laser spot-size seems also to be beneficial in reducing the angle of the cone within which the protons are emitted from the back of the target thus, achieving a more collimated beam.

In a second parameter scan, we explored the case of gradually increasing the incidence angle of the laser on

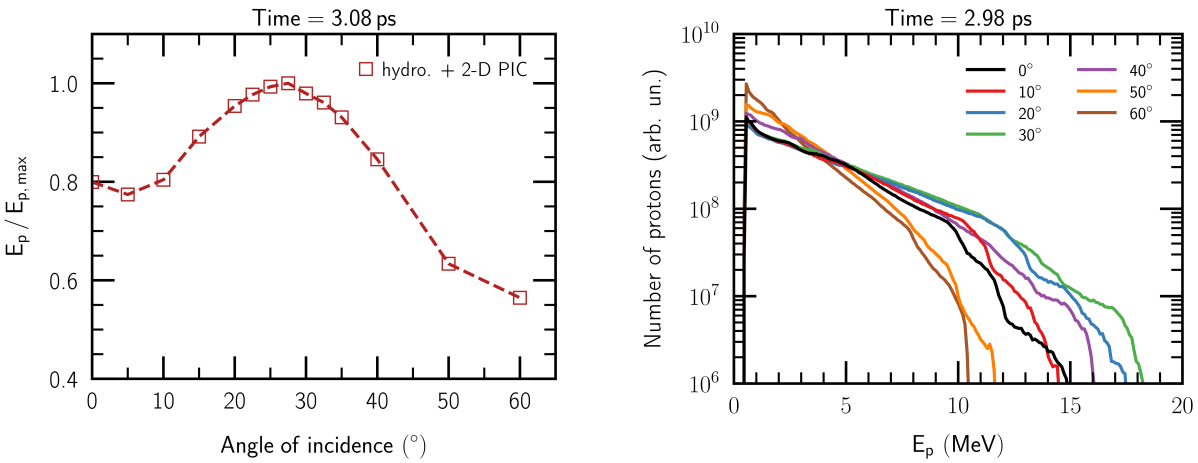

Figure 2: Proton cut-off energy at saturation (approximately 3 ps after the laser hits the front surface of the target) vs the angle of incidence of the laser on the solid target (left panel). The cut-off energies are normalised with respect to the maximum value found at approximately 27.5°. Proton energy spectra at saturation for a series of incidence angles of the laser onto the target (right panel). These simulations consider a 6 µm-thick Al target with a pre-plasma density profile resulted from a hydrodynamic simulation using a preliminary laser contrast curve measured at SCAPA. The laser intensity is $I_0 = 9.97 \times 10^{20}\,\mathrm{W/cm^2}$.

the target from normal incidence to 60°. PIC simulations with oblique targets require a larger simulation box and, thus, significantly more computational resources. Hence, we carried out this set of simulations in two-dimensions. Even though the proton cut-off energy is typically overestimated in two-dimensions, the relative effectiveness of the laser-to-proton energy transfer should be correctly captured by the simulations. Figure 2 indicates that there is an optimal incidence angle of approximately 28° at which the proton cut-off energy is 20% higher than in the case of normal incidence. Increasing the proton cut-off energy is preferable because it leads to higher charge in the exponential part of the energy spectrum below the cut-off.

Once the first set of measurements of the laser contrast at SCAPA was available, hydrodynamic simulations were carried out to model a more realistic pre-plasma density profile, as described in the 12-month progress report. Since that stage, the target density profile resulting from the hydrodynamic simulations was used as an input to the PIC simulations to define the spatial distribution of the particle species at the beginning of the simulations. Figure 3 shows an example of pre-plasma density profile calculated with the hyperbolic tangent function in comparison to an almost abrupt plasma-to-vacuum transition and the more realistic pre-plasma density curve extracted from the hydrodynamic simulation.

We tested the impact of implementing the more realistic pre-plasma density profile into the PIC simulations by comparing the characteristics of the protons generated via TNSA with those resulting from the idealistic model of the pre-plasma used previously. Figure 3 show that the more realistic model of the pre-plasma results in very similar proton energy spectrum to the one obtained with the hyperbolic tangent pre-plasma density at a scale length $L_g = 0.5\,\mu\mathrm{m}$. Consequently, the previous PIC simulations that employed the idealised pre-plasma model at this particular scale-length can be considered to be a suitable model for the experimental conditions at SCAPA. We observed once more that the presence of the pre-plasma in front of the bulk of the target enhances the proton cut-off energy significantly compared to an almost abrupt plasma-to-vacuum transition. However, we notice that different pre-plasma density profiles can lead to similar proton cut-off energies. This can be explained by the very similar number and energy spectra of hot electrons produced when the laser interacts with the pre-plasma.

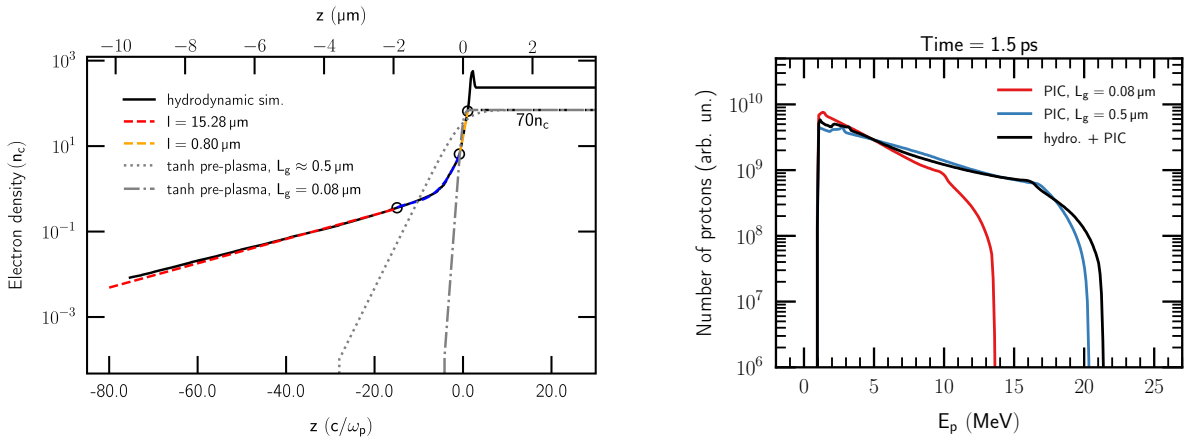

Figure 3: Left panel: Predicted axial density profile on the front surface of the target from the hydrodynamic simulation compared to the idealised tanh model for a couple of scale-lengths L_g. A typical double exponential scale is shown to form during the pre-pulse driven ablation. Right panel: Comparison of the proton energy spectra for the three pre-plasma profiles modelled in front of the solid target from 3-D PIC simulations.

The more realistic model of the pre-plasma indicates that the laser contrast at SCAPA results in better conditions for proton acceleration compared to a scenario with high-contrast and no pre-plasma formation. Under these, more realistic, conditions, the proton cut-off energy is $\sim$21 MeV. As a consequence, the range of energies in which we are interested for LhARA (14.5–15.5 MeV) falls within the pseudo-thermal part of the spectrum and away from the rapid fall near the cut-off energy.

A parameter scan using 2-D PIC simulations was carried out to explore other pre-plasma density profiles that could potentially increase the maximum proton energies achievable with the SCAPA laser. The scan was guided by a differential evolution algorithm so that it can find the 'optimal' pre-plasma density profiles which result in the highest proton cut-off energy achievable with a specific set of laser and target parameters. The optimisation procedure converged towards a set of pre-plasma density profiles with very similar features. Figure 4 shows the pre-plasma density profile which was found to result in the maximum proton cut-off energy. Firstly, the pre-plasma extends up to $\sim$13 mm in front of the bulk of the target. This indicates that higher proton cut-off energies are favoured by pre-plasmas with long scale-lengths. At the same time, most of the 'optimal' pre-plasma profiles we found consist of a foam-like layer with an approximately constant density of $\sim n_c$ that extends over 60–80% of the total length of the pre-plasma.

To validate the pre-plasma density profile found by the differential evolution algorithm, we carried out a full-scale 3-D PIC simulation for identical pre-plasma conditions. The spectrum shown in figure 4 confirms that significantly higher proton energies can be generated in the presence of a foam-like near-critical-density pre-plasma. In particular, the 3-D simulation indicates that proton energies of up to 45 MeV can be obtained without changing the other laser and target parameters. In addition to the enhancement of the cut-off energy, the optimal pre-plasma we found results in a proton emission opening angle approximately half of the angle found for the case of a shorter scale-length pre-plasma. At higher energies, above 10 MeV, all the protons are produced within a half angle of approximately 100 mrad.

A more elaborate picture of the effect that the pre-plasma scale length has on the propagation of the laser before it reaches the target is shown in figure 5. The two cases highlighted in figure 5 correspond to the case of an optimal pre-plasma density profile and a more realistic one. Each case was simulated in three dimensions. The laser propagation through the pre-plasma, in combination with the kinetic energy density of the electrons

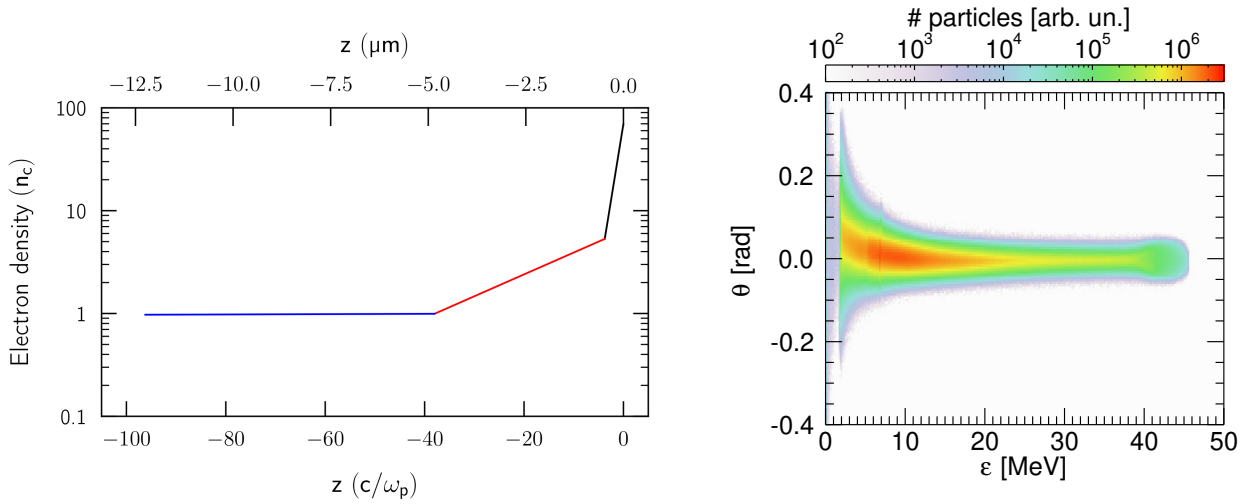

Figure 4: Left panel: The 'optimal' density profile found with a 2-D set of PIC simulations guided by a differential evolution algorithm. An approximately critical density region with a very long scale-length in front of the bulk of the target provides the maximum proton cut-off energy. Right panel: Proton spectrum at saturation for the optimal pre-plasma density profile shown in the left panel. The spectrum is obtained from a 3-D PIC simulation considering a target thickness of 6 μm and a laser intensity $I_0 = 9.97 \times 10^{20}\,\mathrm{W/cm^2}$.

originating in the pre-plasma region, are part of the mechanism that leads to higher proton cut-off energy in the case of longer scale-length pre-plasmas (see figures 4, left panel, and 4, right panel). When a near-critical low-gradient long plasma is present in front of the target, the laser penetrates through the underdense plasma, where it undergoes self-focusing and steepening (figure 5h). Electrons are expeled, forming semi-circular cavities (see figure 5d), when the laser reaches the plasma region where $n_c \leq n_e \leq \langle\gamma\rangle n_c$. In this expression n_e is the electron density, n_c the critical density and $\langle\gamma\rangle n_c$ is the relativistic critical density, where $\langle\gamma\rangle = \sqrt{1 + a_0^2/2}$. The cavities are less well defined in the case of the more realistic pre-plasma with a shorter-scale-length. In the presence of an extended pre-plasma, a larger number of electrons reach higher energies (figure 5i,j).

Finally, in practice, it is challenging to manufacture a high-repetition target that consists of a solid tape with an added layer of foam on the front surface. However, in principle, a near-critical pre-plasma with a long scale-length may be obtained by suitably tailoring the strength and timing of one or multiple laser pre-pulses with respect to the main high-intensity pulse. The work we carried out to find an optimal pre-plasma density profile is planned to continue by exploring the characteristics of the laser contrast curve that are required to generate an optimal pre-plasma profile from a solid target. The rest of the computational resources that are available to us will be assigned to simulations exploring heavy ion (carbon) acceleration. We will evaluate the ion energies achievable under laser and target conditions, optimal for proton acceleration, but also for specifications similar to the ones available at SCAPA.

1.2.3 Progress on high repetition rate ion sources

One of the primary goals for this work package is to develop laser-driven ion sources working continuously at high-repetition rate. This motivates the development of laser instrumentation, targetry and beam diagnostics, as well as the automation of beam stabilisation.

At Imperial College London, work has continued to develop a > 10 Hz ion source driven by the Zhi laser, located in the Blackett Laboratory on the South Kensington Campus. The Zhi laser has been developed specif-

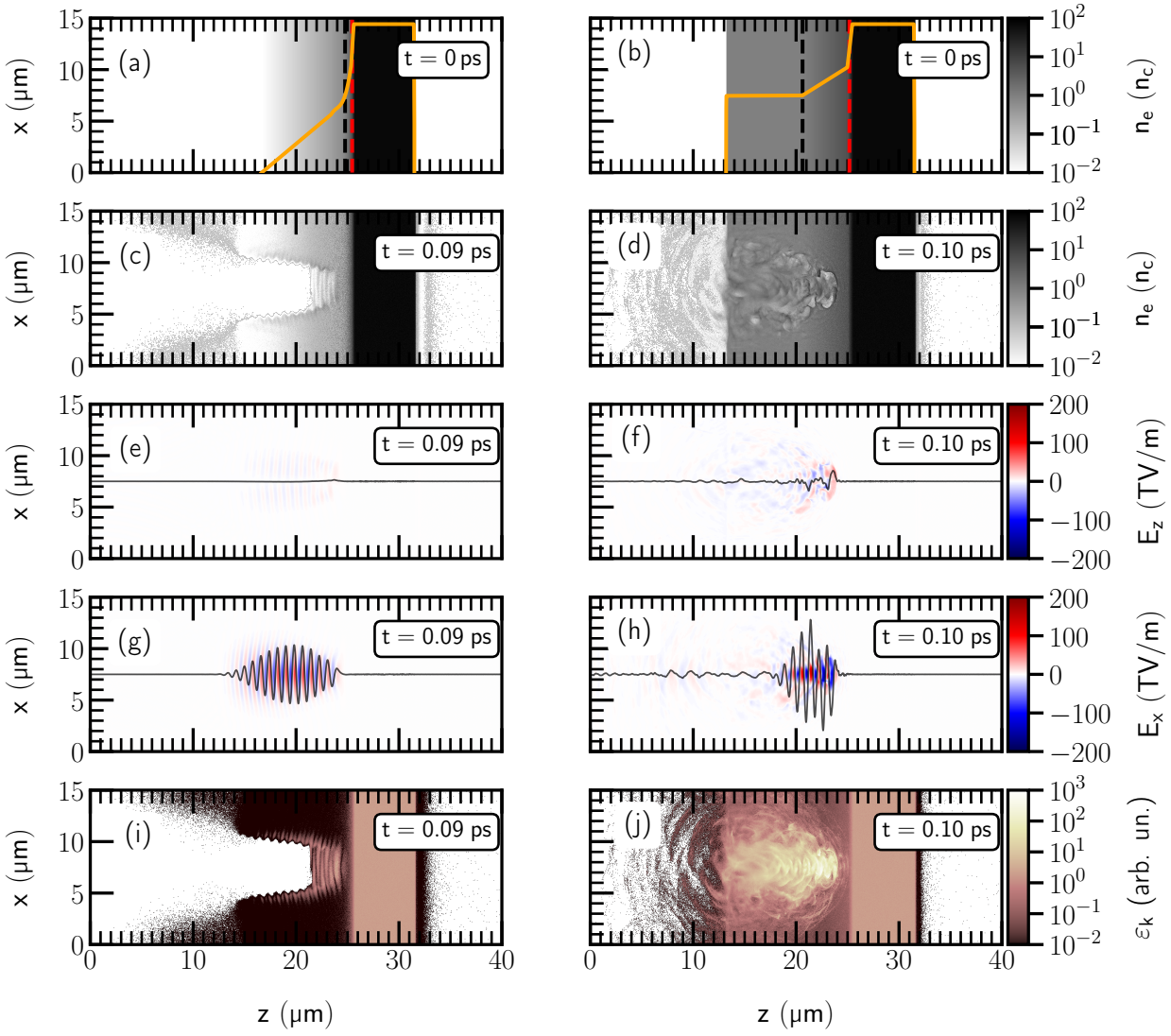

Figure 5: 3-D PIC simulations: (**a,b**) electron density at the start of the simulation, (**c,d**) electron density a short time before the laser reaches the bulk of the target, (**e,f**) longitudinal electric field, (**g,h**) transverse electric field, and (**i,j**) electron kinetic energy density for an Al^{3+} target with a pre-plasma density profile obtained from a hydrodynamic simulation (left column) and the optimal pre-plasma conditions found by the 2-D scan using a differential evolution scheme (right column). The black and red dashed lines in (**a,b**) denote the position of the critical density and the relativistic critical density, respectively. The orange lines in (**a,b**) show the density lineout along the propagation axis of the laser. The black solid lines in (**e,f,g,h**) represent the electric field lineout in the middle of the simulation box.

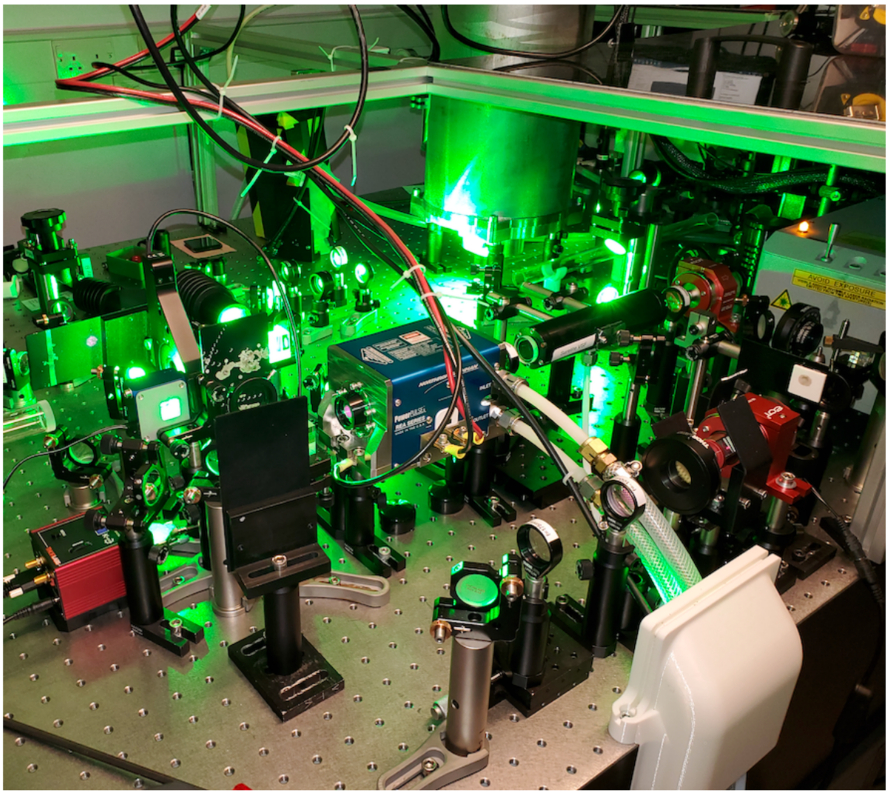

Figure 6: Picture of the final amplifier of the 100 mJ class Zhi laser during operation.

ically for high-repetition rate plasma accelerator research. Progress on the development of the laser-driven ion source has been hampered by various issues with the laser, and particularly poor stability of the oscillator. However, the oscillator has now been replaced and the laser will soon be ready to continue operation. A new amplifier, show in figure 6, has been installed. This laser is capable of delivering an energy of 100 mJ and allowing the generation of proton eneries up to 1 MeV. This is approximately a 50-fold increase in laser energy compared to that used to drive the source previously. During the next six months we will have nearly continuous beam time for the optimisaiton of the source, to test diagnostics and to perform debris studies in a regime more relevant to that envisioned for LhARA.

When running a laser-driven ion source at a high repetition rate, diagnostics that can measure the beam output on a single-shot basis are essential. This motivates the investigation of appropriate scintillator materials for ion beam measurement. We have been developing scintillator-based ion profile and spectrometer diagnostics over a number of years. However, little work has been done to optimise the choice of scintillator or to provide an absolute energy calibration. Therefore, we have been running a scintillator testing campaign using the MC40 cyclotron at the University of Birmingham, as shown in figure 7a. We did initial tests using a 28 MeV beam with excellent spatial quality, as seen in figure 7b. We found good linearity for all the scintillators measured at doses of up 1–10 Gy, see figure 7c. We were also able to generate absolute calibrations for all the scintillator types at 28 MeV. A follow-up beam time will be used to extend the energy calibration to a larger energy range, and to study the afterglow and resolution of the different scintillator types.

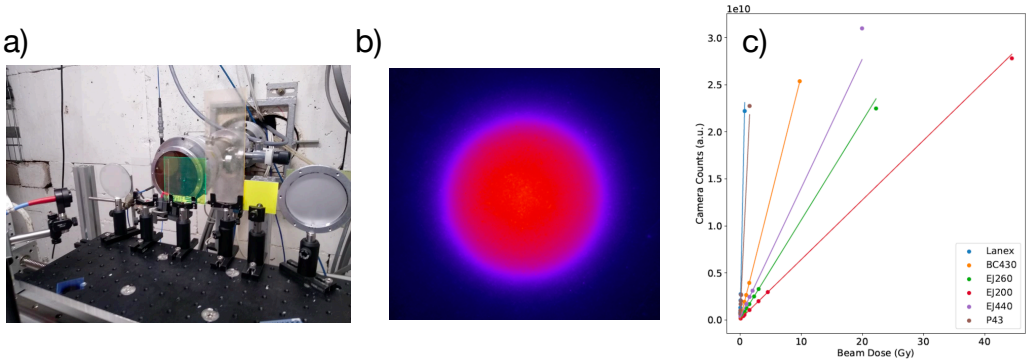

Figure 7: a) the experimental setup at MC40, b) an example beam profile taken at 28 MeV, and c) the linearity with dose of the different scintillators tested.

1.2.4 Development of the SCAPA proton source

Over the reporting period a series of commissioning experiments have been carried out to address the issues identified in the previous report, namely the need to increase the maximum proton energy and the need to operate continuously at repetition rates close to 1 Hz. Through this work we have made significant progress in key areas including beamline lifetime, targetry and source-control system development, as well improvements in the laser itself. Progress in these areas are detailed in the sections below.

The primary output from the last period of testing is the further optimisation of the proton source. The key result is shown in figure 8(a) and (b). In (a) the maximum proton energy measured on the Thomson Parabola spectrometer is shown as a function of calculated laser intensity. Each data point is the average of 25 shots at that laser intensity. The maximum energy observed was around 7 MeV and – importantly – the maximum proton energy is seen to increase and then saturate as the intensity is increased. The increased variability of the maximum proton energy for higher laser intensities is indicated by the increased standard deviation. Although at that time it was difficult to measure the source of the saturation and the increased variability directly, it is indicative of an underlying issue with the laser. Given the target type used we would expect the maximum proton energy to be around 20 MeV.

Detailed investigations were made which confirmed that the laser energy on target, pulse duration, and spot size were within the expected ranges. This left the laser temporal-intensity contrast as a strong candidate for the observed scaling of the maximum proton energy. The laser intensity contrast is the ratio of the peak laser intensity to the intensity of the light that precedes it. This light, although many orders of magnitude lower in intensity than the peak, is sufficient to ionize the front of the target and thus form a pre-plasma. The profile of this pre-plasma is an important factor in determining how the laser propagates to the front surface of the target and how the laser energy is coupled into the electron population that eventually forms the accelerating field for the ions. This expanding pre-plasma also acts to drive a shock wave into the target which can lead to rear surface expansion and decompression of the solid target which can significantly reduce the efficiency of the ion acceleration process. The role of the pre-plasma in optimising the proton source is discussed in more detail in section 1.2.2.

Three measurements of the temporal intensity contrast, made between January and May 2024, are shown in figure 8(b). In the first measurement (shown in blue) from January we see a series of pre-pulses, at approximately -10 ps, -20 ps and -60 ps. There is also a pre-pulse at -330 ps, not shown in this view. Through a series of tests and replacement of optics in the chain, some of these pre-pulses were removed in April; further testing in May 2024 removed all of the pre-pulses except the one measured at -330 ps. Some initial modelling of that remaining pre-pulse indicates that it is not sufficient to ionise the target and thus does not have a signif-

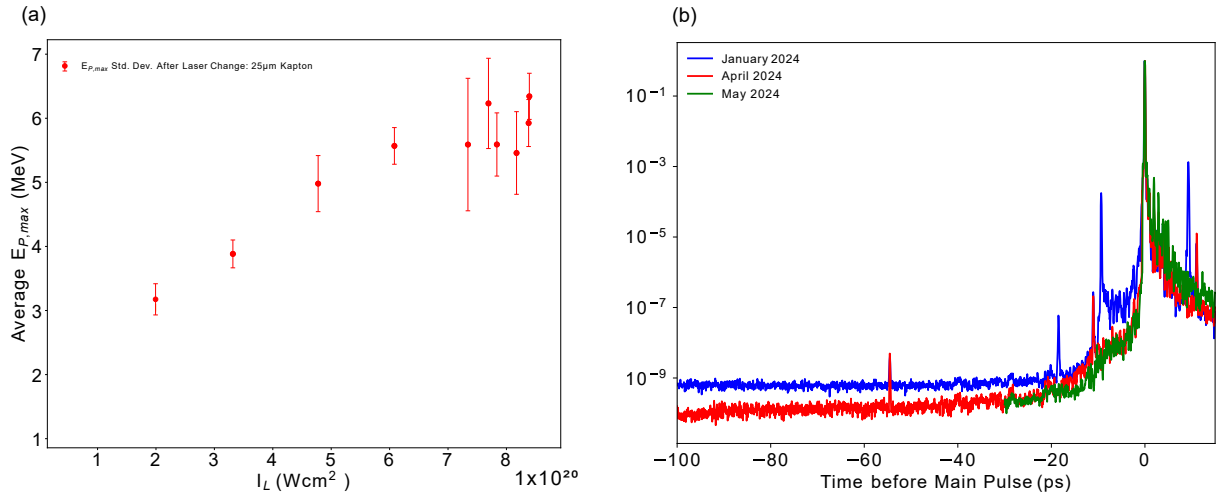

Figure 8: (a) Measured maximum proton energy as a function of laser intensity, averaged over 25 shots for each intensity point. (b) Measured temporal-intensity contrast profile at up to 100 ps before the main pulse. The protons measurements in (a) were taken with when the contrast was in the state shown in the January profile. The profile archived in May will be used in the June 2024 experiments.

icant impact on the front surface conditions. These improvements in contrast are a significant step forward for optimising the proton source on SCAPA and when used we would expect an increase in the maximum energy. The next period of testing, and the first opportunity to use the laser with this updated contrast profile, will take place in June 2024.

The following sections summarise important developments made during the previous 6-month period related to underpinning methodologies for the operation of the laser-driven ion source.

Beamline Lifetime:
A key concern reported in the 12-month report was the role of laser-induced damage forming on the pellicle, ultimately limiting the shot-repetition rate. The pellicle is a very thin <100 μm, transparent film that sits between the focusing parabola and the target to prevent debris from the target reaching and damaging the surface of the parabola. In the initial experiments in July 2023 we made use of a pellicle consisting of TurboFilm, a plastic monomer film used widely for optical protection in astronomy. This material was found to burn rapidly and become damaged after tens of shots, attenuating the laser pulse by up to $\approx 25\%$. In January 2024 we undertook a series of tests comparing this pellicle with a new anti-reflection (AR) coated pellicle purchased from National Photocolor. The results of these tests are shown in figure 9, where the resulting transmission, normalised to measurements made without a pellicle in place, are shown as a function of shot number. Whereas the TurboFilm transmission drops by 15% over 80 shots (and is notably also attenuating the pulse without any damage from the first shot) the AR-coated pellicle starts close to 100% transmission and maintains that transmission within a 5% range over 120 shots. Subsequent measurements with targets in place have shown only minor additional damage forming on the pellicle after $>$ 1000 shots. These results indicate that the AR-coated pellicles are sufficient for operations at full energy at 1 Hz for a sustained period and are now sufficient for the requirements of the source-development phase of this project. Alternative beamline configurations (or targetry) will be considered in the longer term to enable continuous $>$ 1 Hz operations.

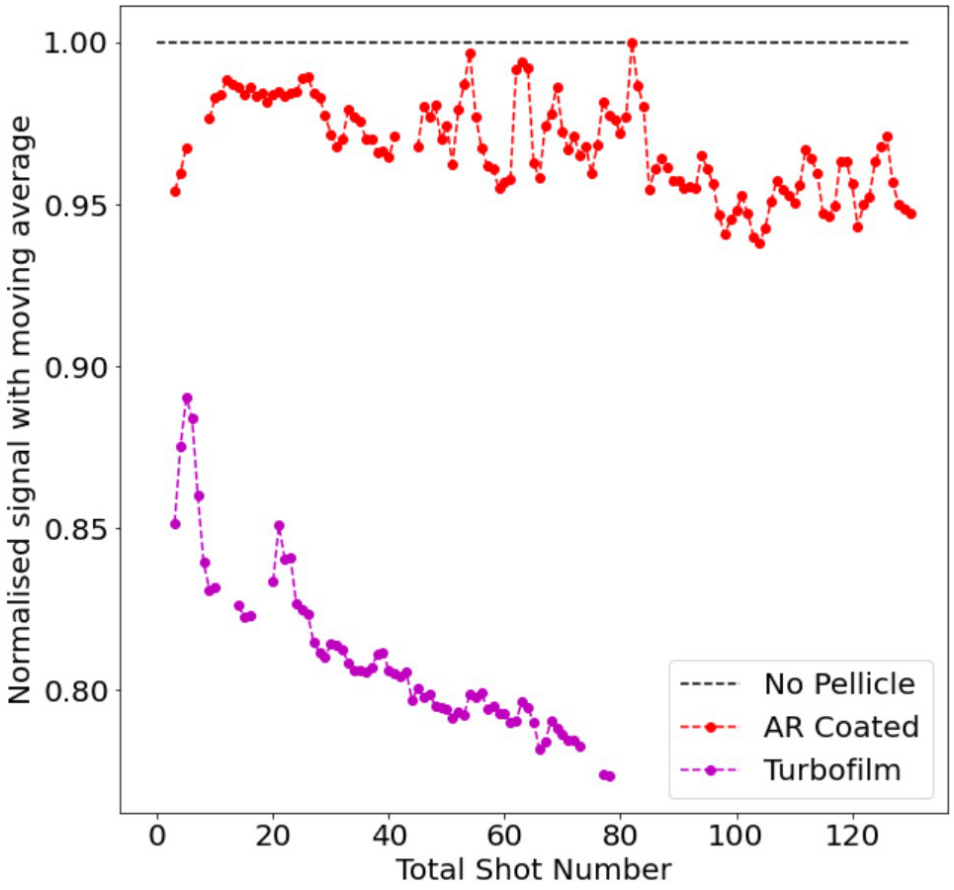

Figure 9: Comparison of the transmission of the laser pulse through the pellicle covering the parabola as a function of number of shots for TurboFilm and a new AR-coated pellicle.

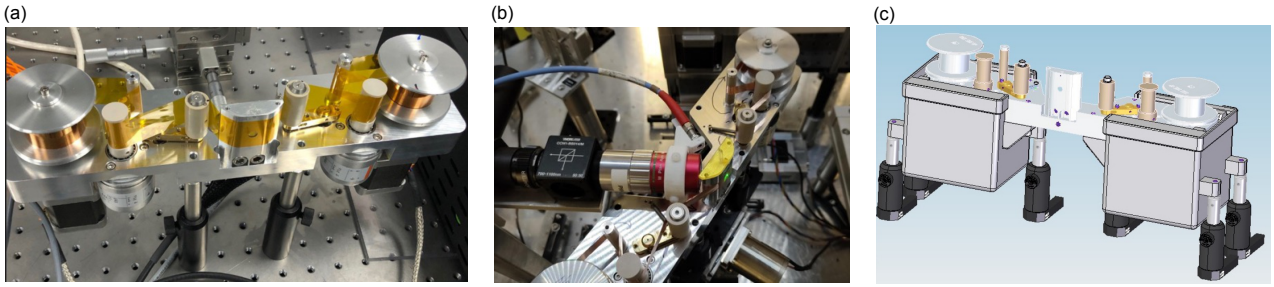

Figure 10: Images of the tape drive target developments (a) Image of the wider tape drive base to enable improved access for the focal spot camera. (b) updated target illumination setup (c) EMP shielding cages for the tape drive motors.

Targetry:
An important insight made during the initial testing of the tape drive target in July 2023 was the difficulty in illuminating and aligning the target at the required angle of incidence (35°). This angle of incidence resulted in a clash (not initially expected but resulting from the tolerance of the CAD model) with the focal-spot camera. As a consequence, only indirect methods of target alignment were possible at that time (via alignment to a reference wire on top of the tape drive). This approach led to an unacceptable uncertainty on the target focal position. A number of changes were made to the design of the tape drive, which are illustrated in figure 10. The base plate of the tape drive was made wider, the tensioning arms of the drive moved further apart and the edges of the face plate were made with a larger angle chamfer. This combination of changes enabled the focal-spot camera to be driven close enough to the tape drive for it to be imaged directly, significantly improving the alignment accuracy. In figure 10(b) changes to the target illumination setup are shown. Now, the infrared alignment diode is injected via a fibre optic placed at 35° to the target, such that the specular reflection is directed into the focal-spot objective. This development has significantly improved the target alignment quality. Finally in figure 10 (c) a planned upgrade to the tape drive system for June 2024 is shown which consists of Faraday cages placed around the tape drive motors and tension encoders. As the source is increasingly optimised on SCAPA (as a result of improved laser-energy coupling into the target) the effect of electromagnetic pulse generation has become disruptive to a number of systems in the laboratory. Recent experience has shown that the tape drive controllers are the most affected by this. The updated design, with Faraday cages included, will be tested in the upcoming June 2024 experiments.

Data Management and Control Systems:
An essential aspect of operating the proton source at 1 Hz is being able automatically to control, stabilise and optimise key input parameters. Through the LPI-Py python library developed at Strathclyde, we have implemented an updated shot-control system during the reporting period. As shown in figure 11(a) this shot-control system enables the experimental team to define a parameter "scan file". This scan file defines the parameters to be changed, the range over which they will be scanned and the number of points in that range. This enables multidimensional grid scans to be defined automatically. From the scan file the individual parameter values for a given shot are written into a "control file" which is then served to individual clients which control laboratory systems to change the laser energy, focusing, pulse duration and pre-heater parameters. The shot is then fired and the resulting data automatically transferred and processed by the in-built data analysis and database functionality of LPI-Py. This control system has also been designed to include machine-learning and optimisation algorithms. Currently a Bayesian optimisation algorithm is included to facilitate fast multidimensional optimisation. Also shown in figure 11(b) is an example image from a new dashboard system built via LPI-Py and the Grafana service. This dashboard system will enable a rapid and remote overview of the operation of the proton source in SCAPA.

1.2.5 Conclusion and brief outlook for next year

Over the next 6 months, work will focus on the outstanding goals for the two-year Preliminary Activity. One significant aim is to generate 15 MeV protons at the SCAPA facility. As described above, significant effort has been put into improvements in the laser and laser-delivery system to enable high energy proton generation. Beam time is scheduled in June to test the impact of these improvements on proton acceleration. We will also continue the scintillator calibration experiments at MC40, with the aim of coming up with a suite of scintillator calibrations which will be optimised for particular beam-diagnostic applications. At Imperial, the new oscillator upgrade for the Zhi laser will enable $\approx$ 1 MeV proton generation at a repetition rate in excess of 10 Hz in the next month. This will allow testing of a variety of instrumentation. Finally, the simulation effort will continue, with added focus on optimisation of carbon-ion production. These studies will inform the development of

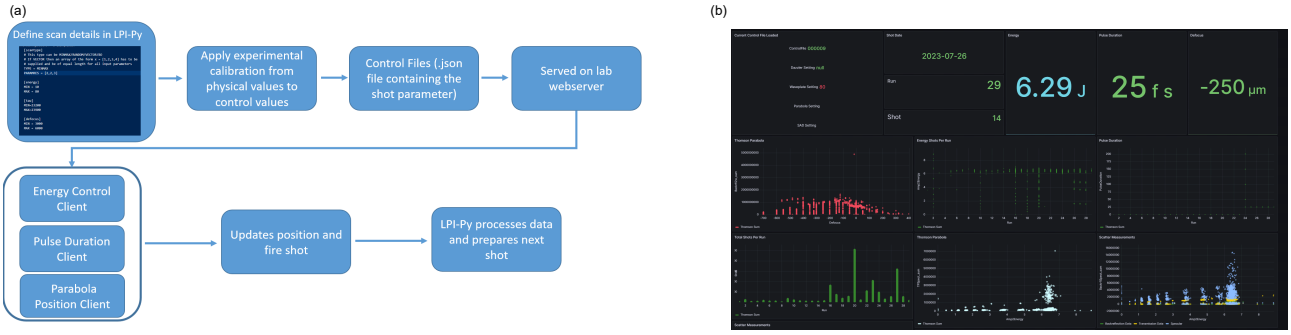

Figure 11: (a) Diagram of the automated data scan control capability. (b) Example image of the Grafana based dashboard system for monitoring source performance.

experimental investigations of carbon-ion production for LhARA.

1.3 Work package 1.3: Proton and ion capture

1.3.1 Background

The object of work package 1.3 is to inform the design of a standalone Gabor lens test-bench. It is envisaged that this would be a test-bench capable of confining a non-neutral plasma (NNP) with space-charge in the low kV range which could be interfaced with a suitable ion source to demonstrate focusing. As previously reported [1, 4], several factors have resulted in significant delays. External administration delayed the appointment of the PDRA who now has responsibility for both the numerical simulation and experimental campaigns. This has resulted in the work being around 1 year behind schedule. The rapid progres made now that the PDRA is in post is summarised below.

1.3.2 Progress

The primary focus since the appointment of the PDRA has been the investigation of plasma confinement using the existing Swansea positron beam-line shown in figure 12. As a consequence, progress on the simulation campaign has been limited over the reporting period.

Plasma loading

Plasmas containing up to 300×10^6 electrons are routinely collected using the trapping scheme shown in figure 13. In this scheme the electrons are trapped both by scattering from the beam into the well and by the cutting of the DC beam when the hold potential is applied. The number of trapped electrons can be controlled by varying the accumulation time as shown in figure 14.

Early electron loads showed significant instabilities resulting in short lifetimes. It was found that this could be controlled by varying the vertical position of the electron gun such that the plasmas were initially loaded as close as possible to the axis of the trap. The optimum position has been found such that a minimal diocotron motion is excited for short times.

New density diagnostic

The existing beam-line was built to operate with low numbers of positrons, so the available diagnostics were ill-suited to the high numbers and densities of electrons used for these NNP studies. Further, the existing multi-channel plate (MCP) suffered from damaged regions which made interpretation of the radial profiles difficult.

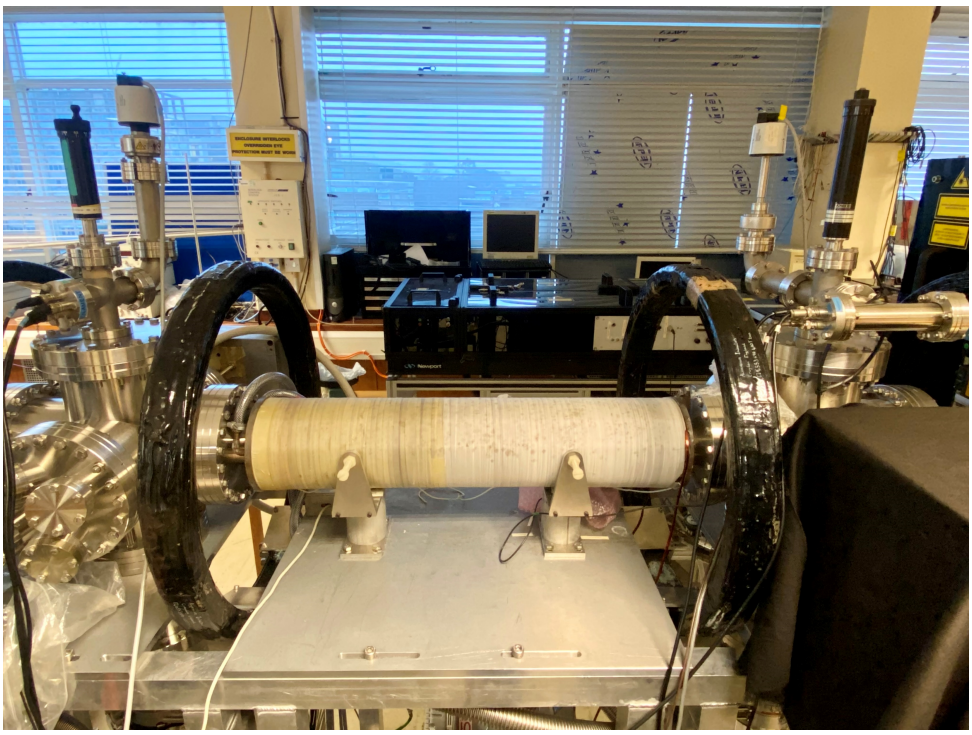

Figure 12: A photograph of the section of the positron beam-line used for these studies.

The MCP has therefore been replaced with a suitable P43 phosphor screen which has a larger dynamic range for the plasma parameters of interest. Example images are shown in figure 15.

Rotating wall application

Since the 1990s, the confinement and control of high-density NNPs has been achieved using the rotating wall (RW) technique. The first demonstration of the technique exploited a magnesium ion plasma [16]. The RW technique requires a length of the ring electrode to be subdivided azimuthally into a number of segments. A sinusoidal voltage is applied to each electrode independently such that the difference in the phase of the sinusoid applied to each individual segment produces a rotating dipole/quadrupole potential near the centre of the cylinder defined by the ring of segments. Two distinct plasma interaction regimes exist depending on the amplitude of the RW and the available cooling mechanisms. The first is the "weak-drive regime" in which the rotating potential is coupled to a plasma-wave (Trivelpiece-Gould mode) and the second is the "strong-drive regime". In the latter the plasma rotation frequency matches the RW frequency and is given by

$$f_p = \frac{n_e e}{4\pi\epsilon_0 B}, \tag{1}$$

where n_e is the plasma density and B is the magnetic field strength. The strong-drive regime therefore offers control over the plasma density.

Experiments on the Swansea system using the RW alone with no additional cooling were conducted. A scan of the RW frequency, figure 16, shows that an interaction with the plasma occurs at frequencies which are consistent with the electron densities estimated from particle-number measurements, radius and the electrode lengths as given in table 1. The use of the RW results in an increase in trapped charge with a maximum increase observed at $\sim$ 21 MHz. The electron plasma in these experiments was in the form of a diffuse cloud. It is believed that the increase in number is due to ionisation of the background gas in the 5×10^{-9} mbar vacuum.

To improve the impact of the RW, CO_2 was admitted to the vacuum chamber at a pressure of 1×10^{-7} mbar to

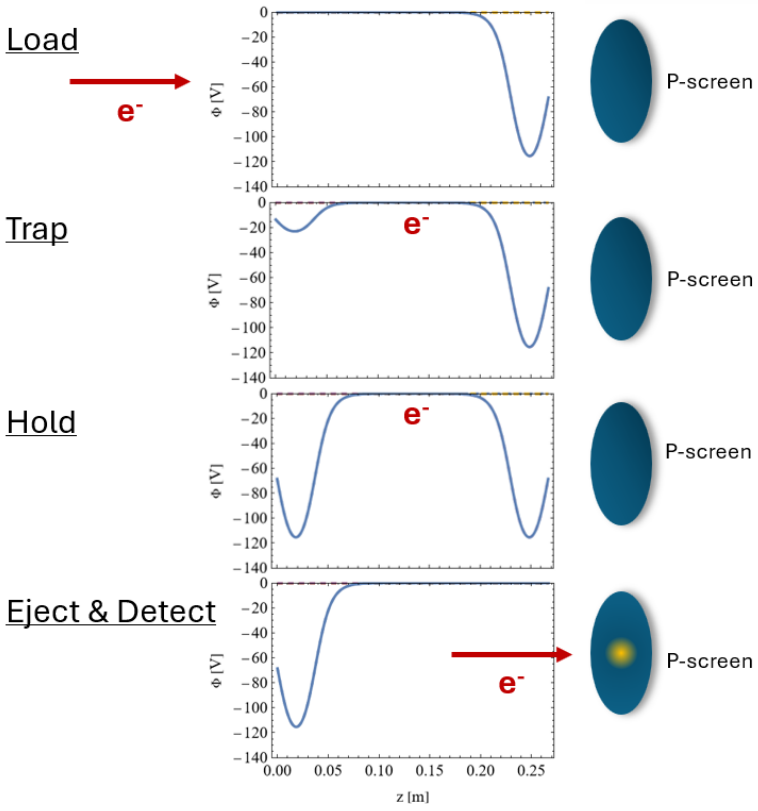

Figure 13: The trapping sequence used for the trapping of a non-neutral plasma of electrons. Initially, electrons are permitted into the potential well before the entrance potential is lowered preventing further accumulation of charge. The clouds are then ejected by lowering the confining potential before impinging on the phosphor screen for detection.

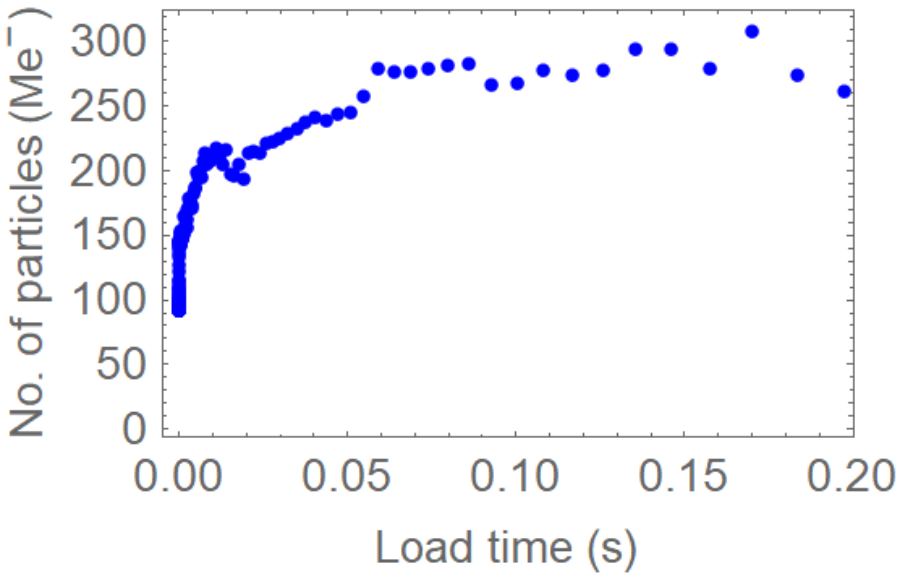

Figure 14: The number of electrons accumulated as a function of time. A fraction of the beam is trapped by the cutting of the DC beam when the hold potential is applied and hence there is a 100 Me- offset.

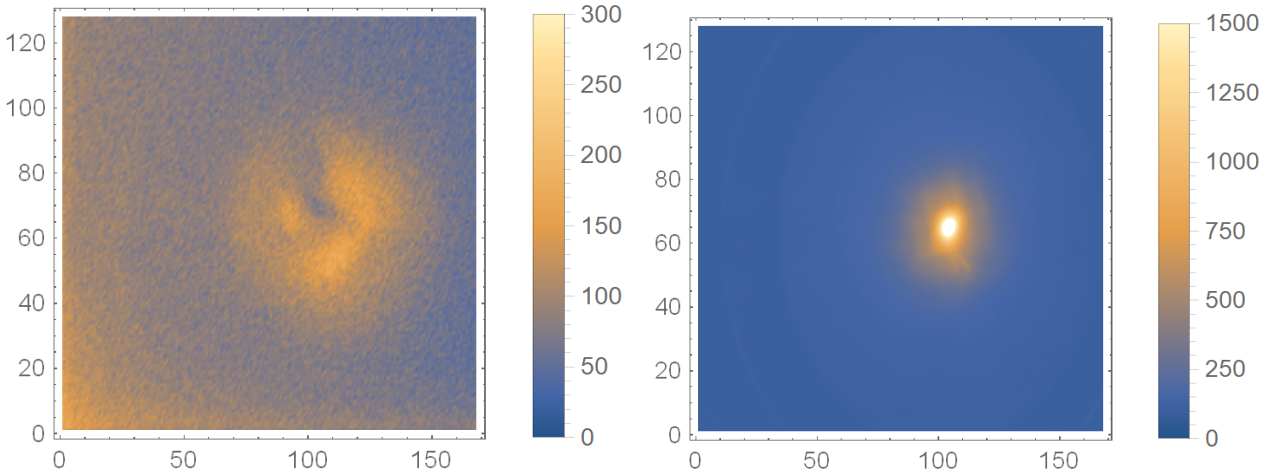

Figure 15: (Left) Example radial profiles obtained with the high-gain MCP showing saturation as well as damage. (Right) The radial profile of a similar plasma obtained with the new phosphor screen.

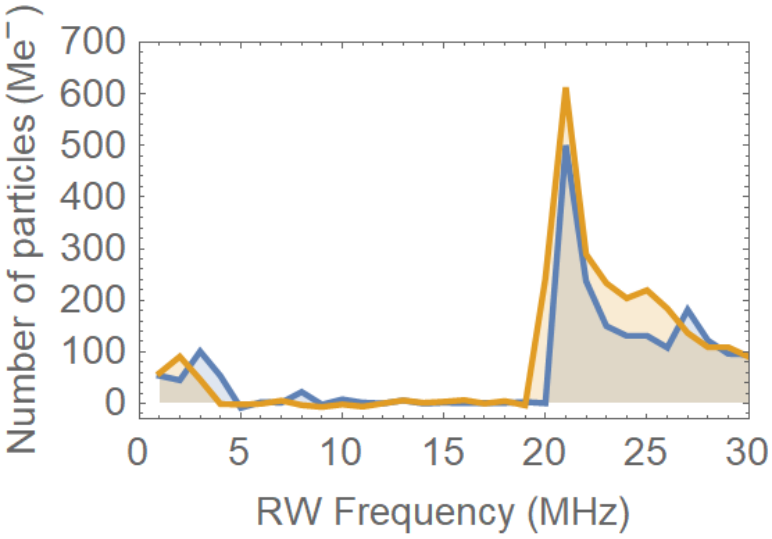

Figure 16: The number of trapped charges as a function of RW frequency without cooling gas. Following a 1 s load, the RW is applied for 1 s with 1.9 V_{pk-pk} before being ejected. The RW is applied in both the clockwise (blue) and counter-clockwise (yellow) directions yielding similar results.

Table 1: Estimated plasma parameters.

Particle number	256 M
Plasma radius	0.85 mm
Plasma length	193 mm
Plasma frequency	20.9 MHz

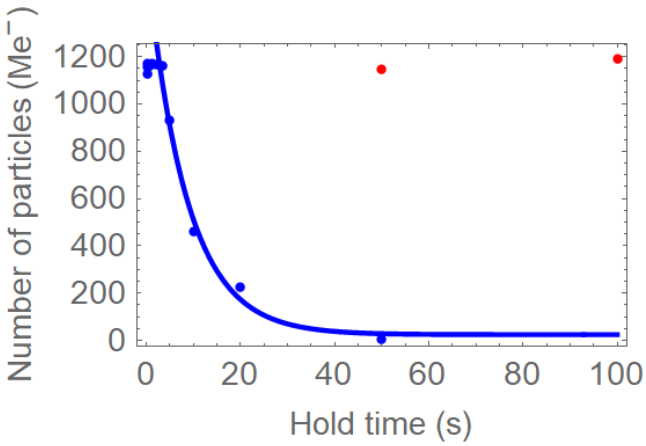

Figure 17: A lifetime curve showing the charge within the trap as a function of time. In the case of the blue points the RW was turned off after 5 seconds of application. The line is a fit of the form $A\exp(-t/\tau)$ with lifetime $\tau = 8.4 \pm 2.5$ s. Keeping the RW on results in an apparent steady state indicated by the red dots.

cool the trapped electrons. This reduces the lifetime in the trap to 8.4 s as shown in figure 17, due to scattering on the gas. A frequency scan of the RW shows additional features, see figure 18. Crude calculations indicate that, in this configuration, the electrons will have a cooling time in excess of 0.1 s. With the addition of CO_2, NNPs have been observed with a finite radial extent as shown in figure 19. In this case the plasma contained a total of 1.2×10^9 electrons with the bright region in the figure indicating a radial extent of 0.8 mm. With an estimated length of 20 cm this yields a density of $10^{14}\,\mathrm{m}^{-3}$. The maximum charge which can be confined by a magnetic field, B, is the Brillouin density limit given by

$$n_B = \frac{B^2}{2\mu_0 mc^2}, \tag{2}$$

which – at the 400 G magnetic field used in these studies – is $7.8 \times 10^{15}\,\mathrm{m}^{-3}$. Hence, we have trapped a significant proportion of the Brillouin density limit.

The plasma appears to be in a steady state with stable confinement demonstrated over 100 s. Further investigation is necessary to determine whether we are operating in the RW strong-drive regime.

1.3.3 Outlook

With the demonstration of the required techniques, we are working towards systematic studies of our trapped plasmas using our new diagnostic tools. To quantify plasma parameters more accurately, we are undertaking a systematic campaign to calibrate the response of the phosphor screen using the Faraday cup. A plasma-temperature diagnostic will also be implemented. With cross-calibration of these diagnostics, we will be able to determine the self-consistent plasma equilibrium using an updated Poisson-Boltzmann solver. These tools will be critical to the diagnosis of large-radius plasmas that image outside the aperture of our diagnostic station and will allow more focused studies on improvements to the plasma-loading scheme. Further, our advances in stable, on-axis loading give us a good starting point to investigate the loading of larger plasmas using different potentials, electron gun operating points and electron gun locations. As work progresses, the new diagnostics will guide investigations of the large operational space of the RW plus cooling gas system. The quasi-equilibrium state achieved while operating the RW will be investigated to estimate the ionisation rate and identify the fate of ions.

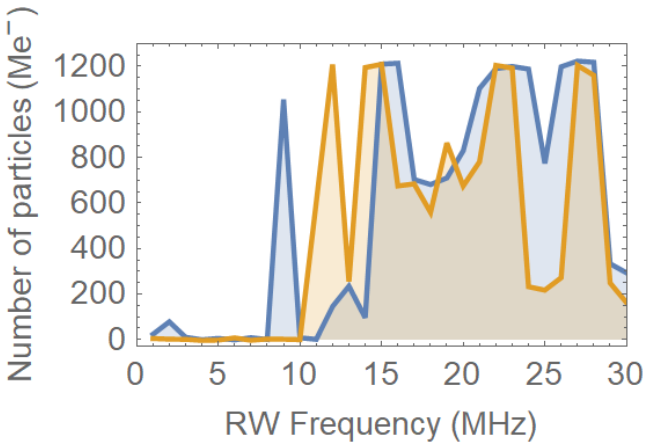

Figure 18: The number of trapped charges as a function of RW frequency with CO_2 cooling gas at a pressure of 1^{-7} mbar following the same procedure as in figure16. There is a marked difference in the behaviour when the RW is applied in the clockwise (blue) versus counter-clockwise (yellow) directions, particularly around 14 MHz. The plasma rotation is in the counter-clockwise direction as defined here.

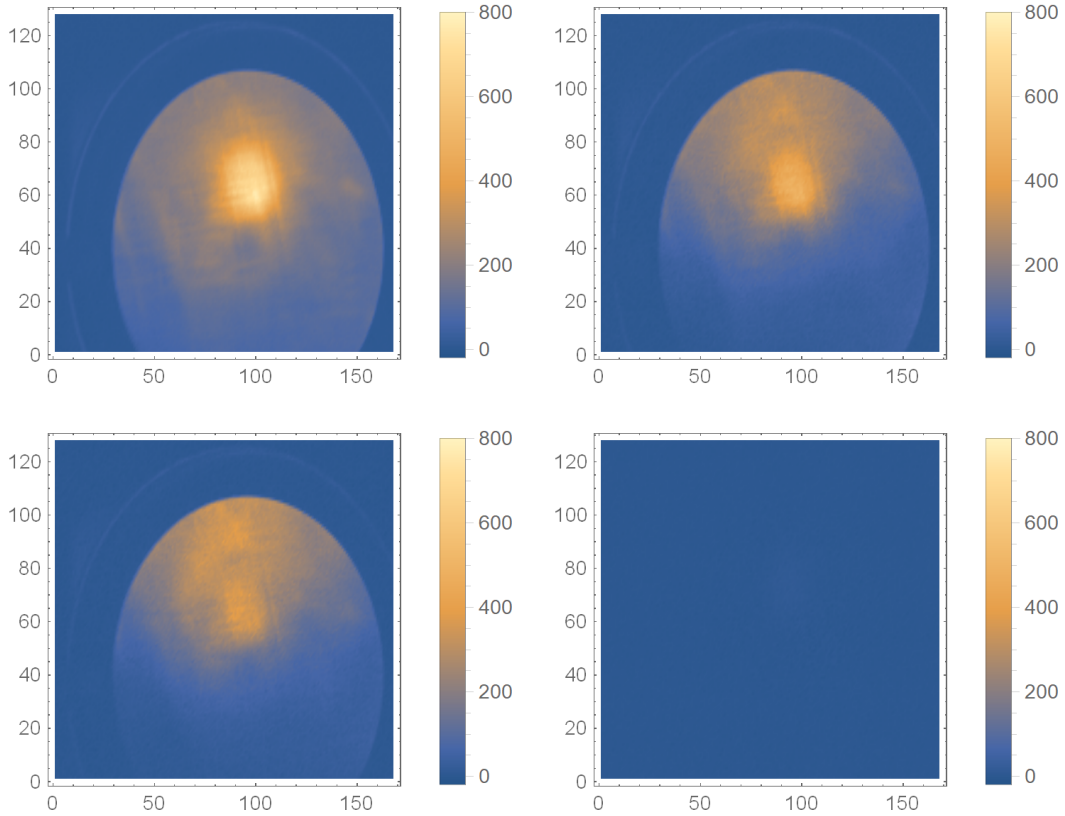

Figure 19: An example of a plasma when the rotating wall is applied for 1 s (top-left), 50 s (top-right) and 100 s (bottom-left) at a frequency of 14 MHz and an amplitude of 1.9 V_{pk-pk}, showing the area with increased plasma density. The number of electrons in the plasma in figures (top-left), (top-right), and (bottom-left) are 1195 Me^-, 1145 Me^-, and 1192 Me^-, respectively (bottom-right). After holding for 1 s without the application of the RW the plasma is not visible on this scale.

Future experimental work

The following experimental investigations will be undertaken:

- The RW technique still has a very large parameter space to be investigated (e.g. RW amplitude, frequency and time) as well as the cooling gas pressure;
- Chirping of the RW frequency such that rotation frequency (and hence density) of the plasma is manipulated;
- Calibration of the phosphor screen image intensity vs charge density;
- Implementation of a Plasma temperature diagnostic;
- Off-axis loading of electrons to produce plasmas with a large radial extent; and
- Further studies to improve the lifetime and stability of the trapped plasmas through the addition of a new translation stage allowing positional control of the solenoid.

1.4 Work package 1.4: Real-time dose-deposition profiling

The objectives for Work package 1.4 are the development of a Geant4 [17–20] Monte Carlo simulation component of a forward model and the development of a k-wave simulation component of the same forward model. These objectives together enable the principal task for the Preliminary Activity phase, which is the detailed design, including identification of potential suppliers of components, of an experiment to prove the principle of ion-acoustic dose-profile measurement to be executed during the preconstruction programme which follows the current Preliminary Activity.

No researchers were resourced for work package 1.4 in the grant for PA1, the work instead being carried out by research students leveraged from outside the PA1 funding. A summary of progress during the current reporting period is provided below.

1.4.1 Review

Overall, encouraging proof-of-principle results have been presented by other groups, indicating detectability of ionacoustic and x-ray-acoustic signals for transient deposition of dose in water, in phantoms and in vivo [21]. As expected from first principles, the frequency content of the emitted acoustic waves depends on a combination of radiation-pulse duration and the spatial-frequency structure in the dose distribution. Groups unable to generate the very short pulses expected from LhARA have deliberately employed ultrasound sensors with a centre frequency (e.g., 350 kHz) much lower than normally used for ultrasound anatomical imaging (e.g., 3-7 MHz). Even sensors centred at 350 kHz, however, tend to edge-detect the field of a smooth x-ray field (e.g. [22]). Superior signal to noise ratio and structure is expected from LhARA, although the evidence from the literature is that we can expect ion-energy dependent high-frequency contributions from the Bragg peak region but largely ion-energy independent low-frequency contributions from the plateau region of the dose distribution upstream of the Bragg peak. Extremely broad bandwidth sensors will therefore be required if all features of the dose map are eventually to be reconstructed. Our workplan, including signal bandwidth studies and reconstruction algorithm development, remains novel and promising.

1.4.2 Monte Carlo part of the forward model

Simulation of current beam line and smart phantom:

A collaboration has been established with the Ludwig-Maximillian (LMU) University Munich, with a view to conducting an experiment using their LION beam-line to demonstrate the ion-accoustic technique using the SmartPhantom and the existing acoustic detectors and camera system. This represents a major but highly positive departure from the workplan described in the original proposal. The demonstration experiment is now scheduled to take place in 2024.

BDSIM was used to simulate the laser-driven LION beam-line directed into the SmartPhantom. A pair of orthogonal quadrapole magnets will be used for focusing. Starting with 10^6 particles, about 50% remained after passing through the magnets, 20% remained after divergence loss in a vacuum path and 4.5% (45000) were left at the exit window after collimation in air for entrance into the SmartPhantom. The energy spectrum of protons at the exit window peaked at about 21 MeV with a full width at half maximum (FWHM) of about 1.4 MeV. The beam at this point was asymmetric in diameter with a FWHM of about 0.67 mm in the x direction and a about 0.37 mm in the y direction.

Geant4 was used to simulate particle transport in water within the SmartPhantom in an aluminium box and a Kapton entrance window at the end of a cylindrical air-filled port into the phantom, producing a 3D deposited-energy distribution with a Bragg peak 4 mm from the Kapton window and a beam at the Bragg peak of FWHM diameter about 1.5 mm in the x direction and about 0.9 mm in the y direction. This dose distribution, assumed to be present for about 40 ns, was used as the input to the k-Wave part of the forward model (see below).

Four planes of scintillating fibres, an essential part of the SmartPhantom design for the planned validation experiment, were incorporated in the Geant4 simulation. Each plane consisted of 33 polystyrene fibres each of length 10 mm, 250 μm diameter, with an array pitch of 300 μm and hence a gap between fibres of 50 μm, forming a sensitive area of $10 \times 10\,\mathrm{mm}^2$. The simulated energy deposited in this fibre array suggested that up to 5 fibres will be illuminated. With fibre planes positioned at about 0, 1, 2, and 3 mm from the centre of curvature of a hemispherical acoustic sensor array (see below), the Bortfeld equation appeared to provide a good fit to the scintillation signal, representing an excellent pulse-specific reference against which to compare the deposited-dose profile reconstructed from the ionacoustic signal. Prototype scintillating-fibre planes have also been successfully constructed to this design, with fibres wound on plastic-printed and aluminium frames.

As mentioned below, k-Wave simulations showed that simultaneous ionacoustic and scintillating fibre measurement of the pulse-by-pulse proton dose distribution will not be possible due to the acoustic wave distortion introduced by the fibre planes. Therefore, the scintillating-fibre detectors will be used to calibrate the response of the liquid scintillator which will be used to determine the deposited energy distribution for comparison with the acoustic mesurement.

A liquid scintillator (UltimaGold XR) consisting of 2,5 diphenyloxazole and 1,4 (2-methylstyryl)-benzine in a combination of various solvents was identified and shown to be miscible in the SmartPhantom tank water. Non-sequential ray-tracing simulation (Ansys ZEMAX OpticStudio) was used to study the quality of the reconstruction of the deposited-energy distribution using two CCD cameras. The optical simulation included consideration of the black anodised inner surface of the phantom (having 5% reflectivity, split 80% Lambertian diffuse scattering and 20% specular reflection) to provide expected. Linearity and dynamic range of the CCD camera were calibrated. Recent progress in developing this liquid scintillator reference method has included prediction of the reconstruction performance using two cameras positioned orthogonally on the SmarPhantom shown in figure 20.

The source of scintillation photons was modelled as a line of elliptical elements along the MC-predicted deposited dose distribution, each emitting photons isotopically. The intensity and number of photons were weighted by the Geant4 predicted energy deposited in each 0.5 mm long elliptical cylinder. Some loss of resolution was observed due to chromatic aberration in the optics, which may be corrected using interference filters. Measurements using transmission spectrophotometry indicated that the absorption peak of the scintillator (below 400 nm) did not appear to shift much when mixed with water at the proposed concentration although attenuation above about 450 nm was increased from near zero to about 38% of the peak, near constant with wavelength, possibly due to scattering by the emulsion formed. Further work is planned to explore the impact of this, develop optical magnification correction procedures, include realistic pixel size and noise, investigate the optical effects of having an acoustic sensor within the scintillator volume, determine the sensitivity to an intensity cut-off (0.1% of peak at the moment), determine whether further opimisation of the optics is helpful

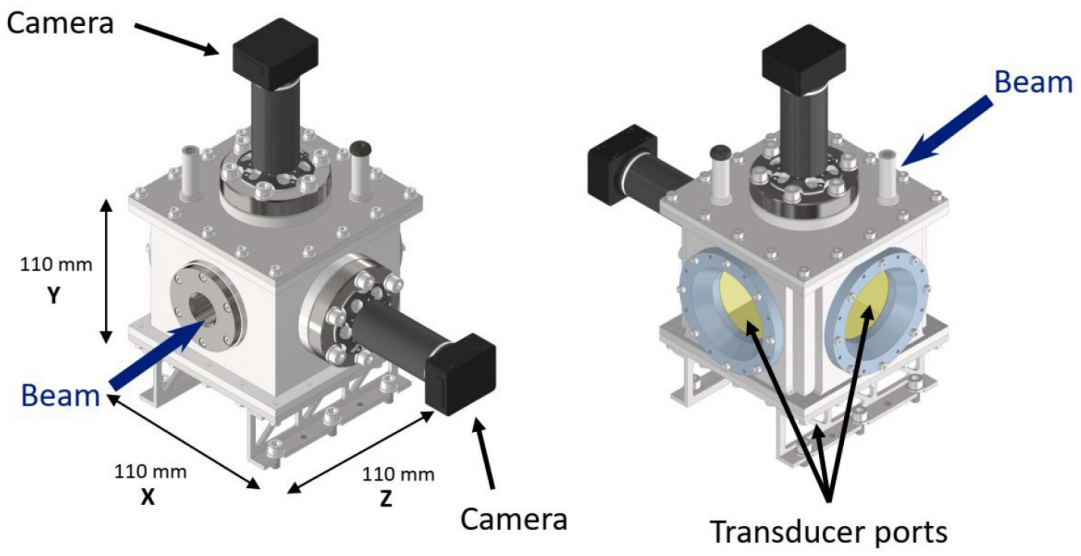

Figure 20: Two views of the SmartPhantom design.

and develop a system to help optical focusing.

The reconstructed dose maps agreed well with Geant4 results, indicating that performance should be sufficient for the optical method to act as a reference for pulse-by-pulse validation of the ionacoustic dose mapping technique. Prior to using the liquid scintillator method as a reference in the LMU experiment, experimental validation of this method with the SmartPhantom is planned, which will employ a cyclotron proton beam in Birmingham.

An MRes Cancer Technology project between the Institute of Cancer Research (ICR) and Imperial College London explored an alternative simulation validation experiment that would not require a beam-line. This employed the output of the Geant4 simulation to 3D print thresholded versions of the deposited-dose distribution as plastic moulds. The moulds were used to create pigmented gel phantoms in the shapes of outlines of the dose distribution at two threshold values, for a 70 MeV proton beam of 40 ns duration. This kinetic energy was chosen to create a Bragg peak at a depth suitable for an existing photoacoustic imaging system at the ICR. Each phantom was imaged using one of two available broadband (100 kHz–4 MHz) sensor arrays. A part-circular ring array surrounding the beam was mechanically scanned along the beam axis to explore signals from acoustic waves emitted radially at various axial positions, and a part-spherical cup array was positioned on-axis beyond the Bragg peak to explore signals from acoustic waves emitted down the beam axis from the distal region of the Bragg peak. Signals above a minimum threshold were used to reconstruct images of the dose distribution. The measured distributions were studied in comparison with k-Wave equivalents for two threshold values (5% and 40% of the global maximum dose at the Bragg peak), providing an alternative validation and allowing the overall acoustic signal time-frequency composition to be better understood for sensor elements placed in various locations. Good low-frequency response is necessary for imaging the relatively constant plateau region of the dose distribution and good high-frequency response is necessary for reconstructing and localising the Bragg peak. For the beam diameter expected, the signals detected from radially-emitted acoustic waves agreed well with both analytical predictions and with the simulation, having maximum signal amplitude at a frequency of about 200 kHz. Transducers with bandwidths extending to 100 kHz have been shown to be capable of detecting these signals in practice, and images reconstructed from such signals showed excellent agreement between the measured beam diameter and the true beam diameter, as well as good ability to display the constant dose value in the plateau region of the beam. Flaring of the beam diameter towards the Bragg

peak was clearly visible in the 3D images reconstructed using the mechanically-scanned ring array. The cup array was capable to detect signal associated with the on-axis sharp fall-off of the dose distribution distal to the Bragg peak, which was blurred by the ring array. The ring array was unable to detect signals upstream of the Bragg peak because the unidirectional on-axis laser illumination originating downstream of the Bragg peak, which was strongly absorbed by pigmented gel, did not adequately simulate the ionacoustic experiment. To achieve adequate simulation, more omnidirectional diffuse illumination, as employed with the ring array, would be needed. Nevertheless, the results were strongly suggestive that a 4–5 MHz upper-frequency response would be sufficient for detecting on-axis signals from, and resolving, the Bragg peak for 70 MeV proton beams.

Updated simulation of LhARA and smart phantom:
In preparation for the validation experiment at LMU, further simulations have been undertaken. Modelling of the LION beam line has more clearly defined the asymmetry of the beam and the energy spectrum of the particles at the focus. Investigation of the impact of secondary particles and electrons generated at the source is ongoing. The presence of liquid scintillator, or a 50% dilution of it in water, however, shifted the position of the Bragg peak away from the source by 2.5 mm and 1.5 mm, and reduced its amplitude by 6% and 4%, respectively. k-Wave simulations have confirmed that a detector frequency response with good sensitivity down to 100 kHz is likely to be required and will be sufficient to detect signals from the plateau region of the dose distribution. Good sensitivity to signals in the 3–4 MHz region will be needed and sufficient to detect and see the acoustic structure of the Bragg peak, The consistency of findings between the digital simulations and the photoacoustic experimental simulations described above, lends confidence to the choice of sensors for the upcoming experiment (see below).

1.4.3 k-Wave part of the forward model

Simulation of ionacoustic source, propagation and sensing, and design of array configuration for validation experiments:
To demonstrate the full simulation pipeline, the above 3D deposited-energy distribution was assumed to exist for 40 ns with instantaneous rise and fall. When converted to an acoustic source-pressure distribution using a Grüneisen parameter for water, this rate of change of deposited energy then acted as the source in a k-Wave simulation. Convergence tests demonstrated that a k-wave finite element mesh of 0.1 mm voxels is sufficient for accurate simulation of the acoustic source and the propagating acoustic wave for 20 MeV protons. Movies of the wave travelling away from the deposited-energy distribution showed wave directions and rates of decay in a loss-less medium (water) are qualitatively consistent with a cylindrically diverging wave along the radial direction upstream of the Bragg peak, and pseudo-spherical divergence from around the Bragg peak, due to the proton beam flaring due to forward and small angle proton scattering. Inward propagating waves were also seen from the boundaries of the deposited-energy distribution, as expected. These phenomena influence the bandwidth of the acoustic waves and hence of the acoustic sensor array design, and their further study is likely to be important in a fully optimised ionacoustic system. The testing of the full simulation pipeline was completed with a simulated array of 300 acoustic sensor elements, each a 2 mm diameter disc, placed on a hemispherical surface of 7 mm diameter positioned with its centre about 2 mm upstream of the Bragg peak. These provided simulated detected acoustic signals for preliminary testing of several potential dose-map reconstruction algorithms under noiseless conditions (see below).

Updated simulation of ionacoustic source and development of sensor array specification, as LhARA specifications are developed in other work packages:
This work has continued as described above. In addition, ionacoustic image reconstruction simulations have been performed for the following sensors, all of which will be taken to LMU for use with the SmartPhantom in

the planned validation experiment with the LION beam-line:

- A single-element bespoke purchased piston hydrophone with a frequency response that extends from the MHz range to at least 100 kHz;
- A single element off-the-shelf narrow-band 1 MHz transducer that had already been used successfully at LMU;
- A 5.3 MHz 75% bandwidth linear array borrowed transducer consisting of 192 elements of pitch 0.23 mm and a 3.5 MHz 60% bandwidth matrix borrowed transducer array of 1024 square elements with a pitch of 0.3 mm distributed in four banks of eight rows of elements with a missing row between each bank over an elevation aperture of 14 mm; and
- A single bank of 32 columns of elements with no missing columns over a lateral aperture of 12 mm.

Each of these transducers can be positioned to detect acoustic waces arriving at one of the three SmartPhantom's windows shown in figure 20 above. Reconstruction of the dose distribution generated in simulation indicates that the Bragg peak can be localised and that the edges of dose distribution determined using any of the sensors. However, only the piston hydrophone is expected to be able to detect, and allow reconstruction of, signals from the upstream plateau region. Finally, further simulations indicate that penetration of acoustic waves into the aluminium case of the SmartPhantom and their reflection from the outer aluminium-air boundary may make a non-negligible contribution. Appropriate time-gating, or other processing, may therefore be necessary for optimal reconstruction of the dose maps.

1.4.4 Implementation, simulation evaluation and development of inverse dose-map reconstruction software

Direct ionacoustic reconstruction with handling of sensor array configurations:
Using the sensors arranged in a hemispherical array, three image reconstruction methods were evaluated: iterative time reversal, model-based minimisation, and direct back-projection. The shape of the 3D dose distribution reconstructed using iterative time reversal most closely approximated that of the original deposited-dose distribution, with a shape around the Bragg peak that converged on correct shape after four iterations. Model-based minimisation required more iterations (greater than 5) and never fully converged. Back-projection is a rapid non-iterative method and directly provided a result similar to that of the first iteration of time reversal and arguably superior to the first iteration of the model-based minimisation method. When the hemspherical detector array was used, for higher proton energies, all methods failed to produce an adequate representation of the deposited-dose distribution at beam depths upstream of the hemispherical centre. This was expected as this region is out of the acoustic field of view of the hemispherical detector array and could be corrected by mechanical motion of the array or by compromising on resolution for extended field of view using other shapes of array and/or other sizes and number of elements. For proton energies of 20 MeV and lower, the reconstruction provided a good representation of the deposited energy distribution, even upstream of the Bragg peak. As mentioned above, however, when acoustic-sensor bandwidth was restricted to higher frequencies (3.5 MHz with 60% bandwidth), a much reduced signal was produced, localised to the high spatial gradient regions of the proton dose distribution, as expected.

k-Wave modelling with four scintillating fibre planes present in the SmartPhantom showed extensive disruption of the acoustic waves and reconstructed acoustic pressure distributions that were far from adequate as a representation of the source pressure distribution, even for the basic task of localising the Bragg peak. As a consequence, the plans for scintillation reference mapping of the deposited dose were altered as described above.

Iterative reconstruction methods with angular dependence of frequency content from 4.2 and 4.3:
This activity is due to start Q4 of 2024 or later, because the validation experiment was brought forward into PA1.

Implementation of various dose-map reconstruction programs on Verasonics system:
This activity is due to start Q4 of 2024 or later, because the validation experiment was brought forward into PA1. The Verasonics system will be used to acquire acoustic sensor array data from the LION beam. Dose-maps will then be reconstructed off-line.

1.4.5 Additional experimental work

As mentioned above, experimental work not envisaged in the original bid for funding for PA1, is now planned at LMU, bringing forward the first experimental validation of the ionacoustic method. In preparation for this experiment, transducer arrays (the matrix and linear arrays referred to in 1.4.4.1 above) and a 256-channel ultrasound data acquisition system (Verasonics Vantage-256) and 1024-256 multiplexor will be provided on loan by ICR. The SmartPhantom has been constructed with the two ultrasound viewing ports shown in Figure 20 above, providing interchangeable acoustic access to an orthogonal radial view of the beam and one downstream on-axis view. Experiments were conducted recently at ICR, which demonstrated negligible loss or corruption of signal after propagating ultrasonic waves through the Kapton foil and gel that will be used to acoustically-couple the ultrasound sensors to the liquid in the SmartPhantom. Finally, as mentioned above, prior to the experiment at LMU, an experiment will take place in Birmingham to validate the optical scintillation methods as field reference standards against which to compare the ionacoustic results.

1.5 Work package 1.5: Novel, automated end-station development

1.5.1 Overview

Progress over the reporting period includes: literature review of existing dosimetry techniques; developments of the gas jet profiler to be more suitable for ITRF/LhARA including a beam test at Dalton Cumbria Facility (DCF); the third consultation meeting with emphasis on the high-energy *in-vivo* end-station; simulation of potential end-station components; and the conclusion of undergraduate projects based on beam monitoring for LhARA. These are all covered in more detail below.

1.5.2 Literature review of existing FLASH dosimetry techniques

A comprehensive report on existing dosimetry techniques has been developed and will shortly be finalised and added to the ITRF and LhARA repositories. A short summary of the headlines is included here:

- Ionisation chambers considered a gold standard for conventional dosimetry, are significant in proton and electron dosimetry but face limitations due to ion recombination at high dose rates.
- Diodes suitable for photon and carbon dosimetry, offer high spatial resolution but suffer from radiation damage at high dose rates.
- MOSFETs used for proton, photon, and electron dosimetry, exhibit temperature-dependent dose response.
- Diamond detectors applicable for proton, photon, and electron dosimetry, need to be studied further to determine the energy response and its temperature dependence.
- Faraday cups measure total collected charge with high spatial resolution but these completely stop the beam.
- Fricke dosimeters used for proton dosimetry, provide dose measurements but, at high dose rate, are affected by diffusion of radiation-induced species.
- Alanine is mainly used for photon and electron dosimetry and have decreased accuracy at low doses.

- Radiochromic/radiographic films a gold standard for beam profiling in proton, carbon, and electron dosimetry. The response falls below the linear projection (under response) in high LET fields.
- Polymer gels offer high spatial resolution for 3D dosimetry in proton photon, and electron applications but have a complicated readout machinery.
- TLDs and OSLDs used for photon, and electron dosimetry, exhibit and energy-dependent response and are time-consuming in operation.
- Scintillators suitable for electron and proton dosimetry, provide real-time readout but require energy-dependent correction factors.
- Cherenkov detectors are only used for electron and photon dosimetry.
- Calorimeters applicable for proton, photon, and electron dosimetry, are bulky and are time consuming in operation.

The selection of a dosimeter depends on requirements such as dose-rate dependence, spatial resolution, and application context, especially in advanced radiation therapy. The gas-jet system developed as part of the ITRF/LhARA project, provides a measurement of the beam properties in real time, has a response that dose not saturate at high dose rate, is able to give a 2D beam-intensity profile, and is minimally disruptive to the beam. The technique is therefore a good option for beam monitoring in FLASH therapy and for LhARA.

1.5.3 Gas Jet Profiler Developments

Beam profile measurement experiments at Dalton Cumbrian Facility:
An upgraded gas-jet ionisation profile monitor was integrated into the accelerator beamline at the Dalton Cumbrian Facility (DCF) in Whitehaven. The objective was to conduct proof-of-concept measurements of beam profile and intensity in beams resembling those found in medical-treatment facilities. The measurements encompassed proton and carbon-ion beams of varying sizes, energies, and currents. The results of these experiments highlight the feasibility of such a beam diagnostic and provide valuable insights for its refinement. In this study, the gas-jet monitor is presented as a prospective beam monitor tailored for use in hadron beams.

The integration and testing of the supersonic gas-jet monitor and the measurement of a variety of transverse beam profiles of proton and carbon-ion beams across various beam parameters were successfully conducted. These measurements also point to improvements necessary for the monitor to be able to determine the transverse beam profile in LhARA. The measurement of a nitrogen gas-jet signal using a proton beam obtained after averaging and subtracting the background is given in figure 21. The results obtained at DCF have allowed improved estimation of the performance for LhARA to be made.

Design of new ionisation profile monitor:
The experiment conducted with proton and carbon beams at DCF highlights the requirement for a dosimeter capable of fast detection that is compact enough to be integrated with medical accelerators. The ion-acoustic approach described in section 1.4 has the potential to be developed into a non-destructive, real-time *in-vivo* dose-profile measurement device.

A complementary approach, an innovative ionisation profile monitor (IPM) system, is being developed at the Cockcroft Institute. The realisation of the IPM requires a novel design that is compact and addresses the objectives of field uniformity, background noise reduction, and accounts for recoil and initial velocity effects. The main aim of this development is to reduce acquisition time and thus provide real-time feedback. We designed an IPM and validated it by simulating the electric field distribution and particle trajectories using COMSOL and CST Studio. The 2D distribution of the electric field on the axial plane is given in figure 22, and the particle trajectories and beam profile are shown in figure 23.

The resultant system successfully achieves reductions in both size and complexity, although it also underscores challenges associated with field distortion. Future efforts will concentrate on overcoming these chal-

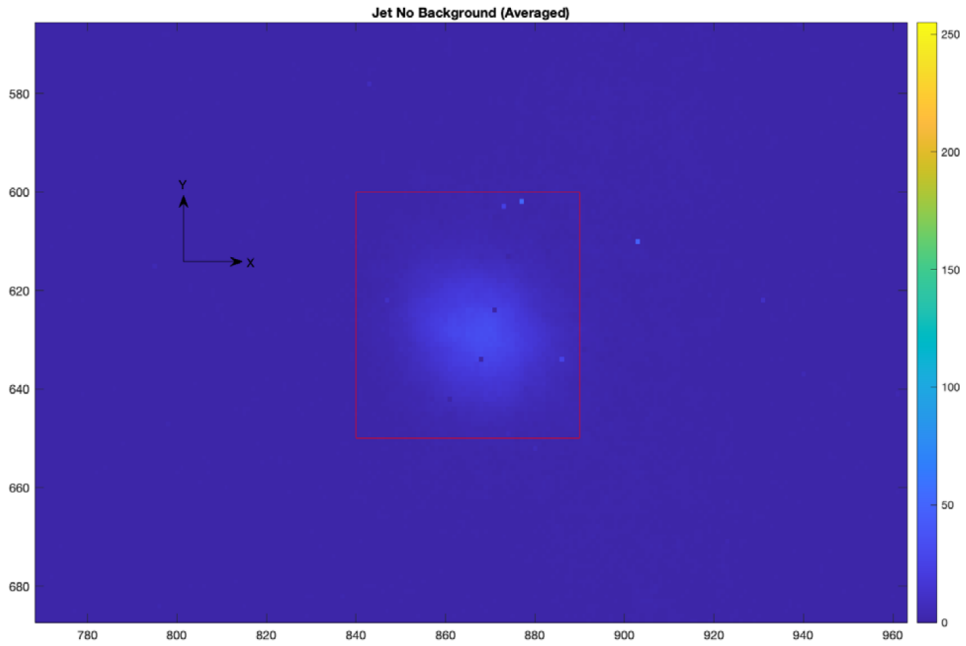

Figure 21: Image of normalised nitrogen gas jet signal, inside the red box, from the interaction with a proton beam, the background is removed.

lenges through manufacturing enhancements and rigorous experimental testing.

Future work:
Planning for an experiment using the modified IPM at the MC40 cyclotron at Birmingham University is being planned for execution in the first two weeks of August 2024. Furthermore, there are plans to expand experimental studies with the gas-jet system at the Scottish Centre for the Application of Plasma-based Accelerators (SCAPA) in Glasgow.

1.5.4 Third user consultation meeting

The third peer-group consultation meeting, which focused on the Stage 2 *in-vivo* end station, was held on the 24^{th} January 2024 at the University of Liverpool. The meeting focused on the legislation and facility requirements for experimental animal research as well as implications of using the facility to assist in the treatment of companion animals. The potential of both sets of irradiation were discussed. Invited speakers Martin Fray of the Mary Lyon Centre and David Killick of the University of Liverpool also fielded questions in an extended question-and-answer session.

The key legislation governing *in-vivo* experiments and the restrictions the legislation imposes are highlighted in the meeting summary document. The recommendations agreed at this meeting have been added to the recommendations gathered from the previous peer-group consultation meetings and are recorded in the summary. The principal conclusion from the meeting is that animals may be provided by external entities (companies, institutes, etc.). However, once accepted into the *in-vivo* facility, the animals must be managed on site and may not be returned to the external entity. Thus, even if the ITRF does not include a complete "animal hotel", provision for appropriate husbandry facilities in an "animal house", co-located with the facility, will be essential. Both M. Fray and D. Killick have agreed to continue their involvement as advisers as the project develops.

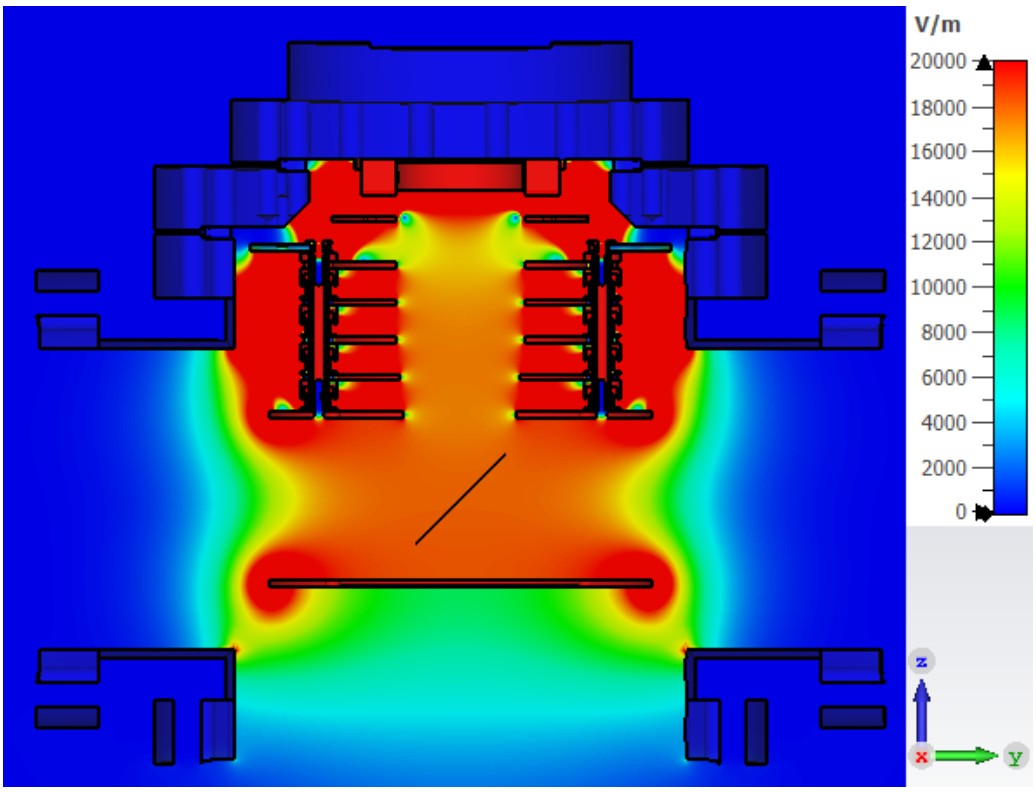

Figure 22: 2D distribution of electric field on axial slice plane for IPM with mounting elements.

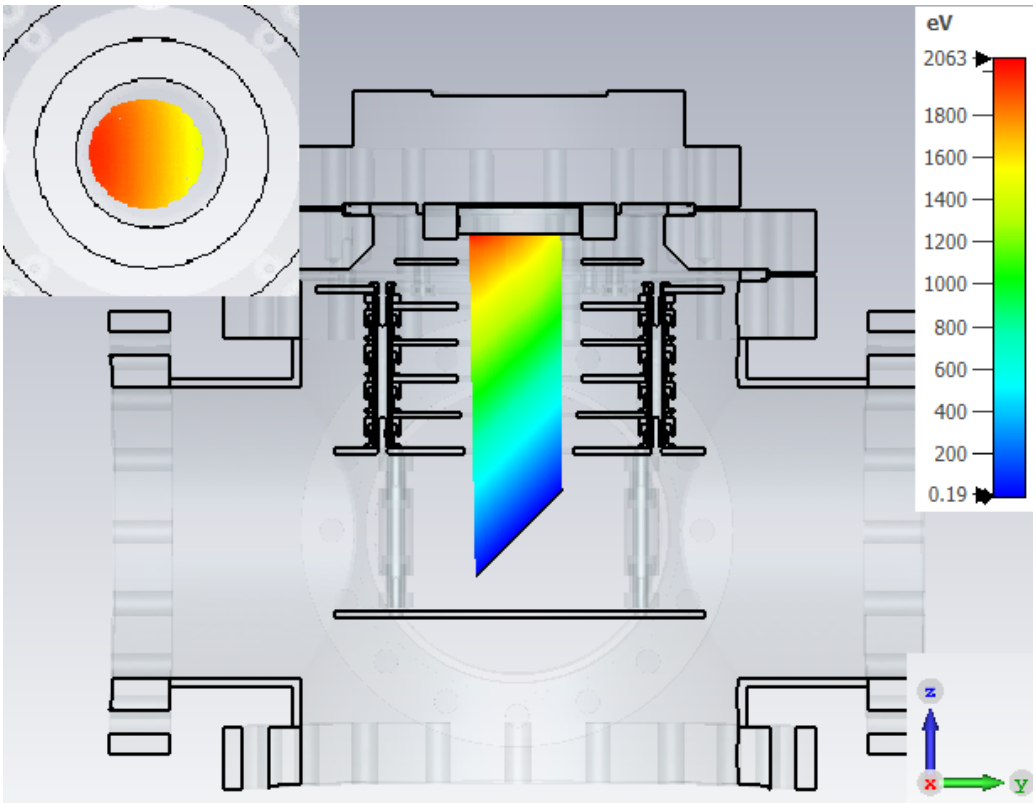

Figure 23: 2D distribution of electric field on axial slice plane for IPM with mounting elements.

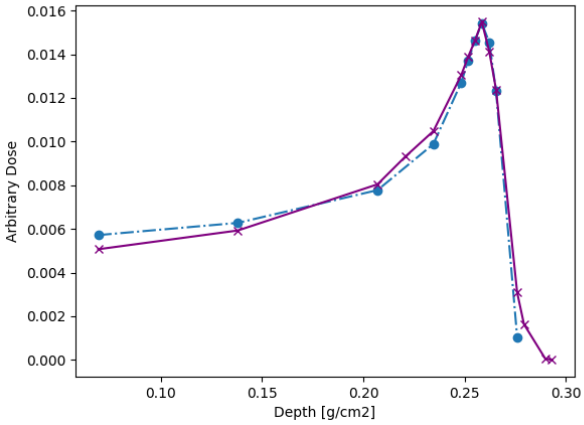

Figure 24: Comparison of experimental range measurements of a 15.5 MeV proton beam incident upon sample (blue) and a dedicated Monte Carlo model of the MC40 cyclotron and G4EndStation for LhARA (purple).

The fourth user consultation meeting will take place later in 2024 at the University of Birmingham. This meeting will focus on the Stage 2 *in-vivo* end-station, but with an emphasise on the user requirements of such a facility rather than the legislative and facility requirements.

1.5.5 MC40 developments and component derisking

The dose-rate capabilities of the MC40 cyclotron have been discussed in previous reports. Over the last six months, the measurements of dose rates up to 2.5 kGy/s using calorimeters from NPL have been submitted for publication. The FLASH delivery system has also been developed. Preliminary measurements, using silicon strip detectors, indicate that the beam can be turned off in less than 70 μs. Further measurements are planned which will include the investigation of the reproducibility and minimum duration of a pulse of protons that can be delivered.

Cyclotron settings have been identified that are suitable for testing dosimeters, components, and the investigation of geometrical effects. A 20 MeV beam extracted from the cyclotron incident upon a scattering system is able to deliver a uniform beam of 50 mm diameter to the end-station/cell dishes. The beam is monitored using a standard ionisation chamber and delivers a 15.5 MeV proton beam onto sample. The Bragg peak in Mylar has been measured (see figure 24) using an Advanced Markus chamber. The energy has been verified using a previously validated Geant4 simulation of the beamline. The simulated Bragg peak calculated using the simulation is overlaid on the data in figure 24 and is in agreement with the data. The projected range of a 15.5 MeV beam from PSTAR is 2.69 g/cm^2, which is also in excellent agreement with the data. The impact of end-station components on the beam parameters will be studied using a Geant4 model of the end station (discussed in the 12-month report). These developments will prove invaluable for work to be conducted in the next six-month period, testing potential LhARA components at the MC40 cyclotron.

GAFChromic films EBTXD and HD-V2 have been identified as potentially useful for single-shot dose measurement and the measurement of dose rate. A student project focused on developing a calibration routine for these films using the 15 MeV beam. At such low energy the potential for under-response of the films (as reported in the literature) needs to be studied. The 15 MeV proton beam is completely stopped by the cell dish. So, by observing the beam halo around the dish, the alignment could be verified. It proved possible to determine the alignment from the hallow provided the scattering of the low-energy protons could be minimised with a suitable geometrical setup.

A second student project investigated the potential use of silicon-strip detectors to measure 1D profiles of the beam. Unfortunately due to confusion regarding detector properties, it was not possible to measure these profiles at the MC40 cyclotron. However, optimal detector properties were identified for a future beam-monitoring system. In addition, a CMOS pixel sensor with the capability to measure single pulses has been designed and manufactured by Nordson Ltd. We hope to test this pixel sensor in the coming months.

1.6 Work package 1.6: Facility design and integration

1.6.1 Radio-frequency cavity

The fixed-field accelerator conceived for Stage 2 is required to deliver a momentum gain of a factor of three, for protons and for ions up to carbon. The design parameters of the RF cavities to be used for proton acceleration are given in table 2. The principal parameters are the frequency range of 2.89–6.48 MHz and the voltage-gain per turn of 4 kV. Two technology choices are being considered for the LhARA FFA cavity: ferrite loaded; and magnetic alloy loaded.

The RF cavity for the FETS FFA, which has similar requirements to the LhARA cavity, is being developed by the ISIS synchrotron RF group. Both ferrite cores and magnetic alloy cores are being considered and measurements of material properties of prototype cores are in progress. The ISIS-FFA and LhARA-FFA design teams are working towards closer collaboration in view of the common issues and synergies between the two projects.

Table 2: Principal parameters for the RF cavities to be used for proton acceleration.

Parameter	Value
Proton RF frequency	2.89–6.48 MHz
Voltage per cavity	4 kV
Bunch intensity	10^9 protons/bunch
Harmonic number	1
Horizontal aperture	65–85 cm
Vertical aperture	7 cm (approx.)

Ferrite-loaded cavity

Figure 25 shows a schematic diagram of a ferrite-loaded cavity. Details of the analysis of this device can be found in [23]. The bias current, I_{gen}, induces a magnetic field in the ferrite discs and is used to modulate the effective permeability, μ'_p. Variation of I_{gen} allows the resonant frequency to be swept over the required range.

The shunt impedance, R_p, of a ferrite cavity is given by [23]:

$$R_p = \omega \frac{N t \mu'_p Q}{2\pi} \ln\left(\frac{r_0}{r_i}\right) = N t \mu'_p Q f \ln\left(\frac{r_0}{r_i}\right) \; ; \tag{3}$$

where the expression for R_p consists of a term purely dependent on geometry, $N \ln(r_0/r_i)$, and a term given by the characteristics of the material, $\mu'_p Q f$. The material term is often quoted by manufacturers and is dependent on frequency (see figure 26 for examples of $\mu'_p Q f$ for different materials). The cavity design requires that $\mu'_p Q f$ be measuremed over the required frequency range and under the high-power operating conditions.

The operation of a ferrite-loaded cavity requires a bias-current power supply, an RF power-amplifier chain, and a low-level RF control system. The bias power supply must be capable of ramping the required current

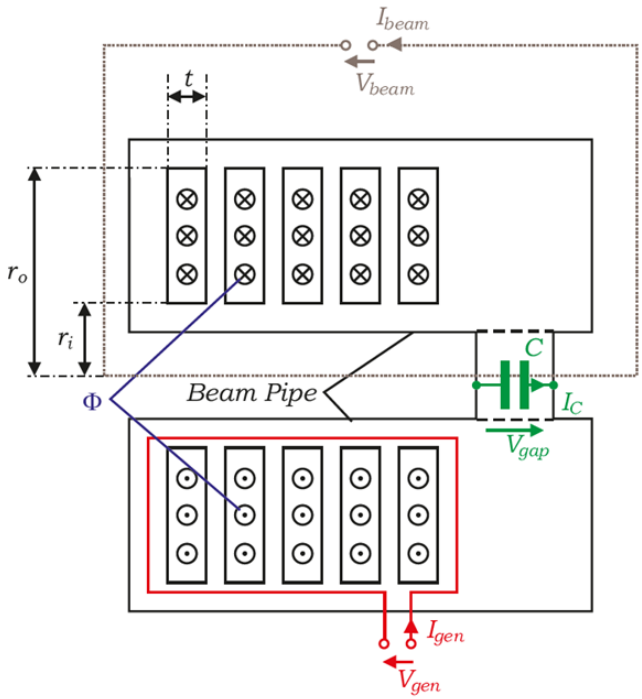

Figure 25: Simplified schematic diagram of a ferrite-loaded cavity [23].

within the period of one acceleration cycle, thereby varing μ'_p.

Magnetic-alloy loaded cavity

Magnetic-alloy (MA) loaded cavities are similar to ferrite-loaded cavities in that they use an inductive core to give a relatively low resonant frequency. In the case of the MA cavity, the permeability and the saturation magnetic field are much higher than for the ferrite cores. This gives the cavity such a large bandwidth that there there is no requirement to use a bias current to sweep the resonant frequency. This simplifies the power-amplifier and low-level-RF systems. However, since the cavity has a low Q value, the power dissipated in the cores will be higher, which would have an impact on the running cost of the cavity.

The magnetic-alloy core is made from a metallic ribbon that has an insulation layer between adjacent ribbons. The ribbon is wound into the shape needed for the aperture of the cavity. The core then undergoes either an annealing or a nano-crystallisation process. Figure 27 shows a schematic of the MA-core cavity for the FETS FFA and figure 28 shows a photograph of a prototype core purchased by the ISIS synchrotron group to measure the $\mu'_p Qf$ of the material. Figure 29 shows the $\mu'_p Qf$ as a function of the RF magnetic field. As can be seen, the MA cores do not suffer from saturation effects such as those observed in the ferrite cores.

Discussion

The ferrite-loaded option requires the magnetic field in the cores stay below the saturation limit. The addition of additional cores will result in a lower magnetic field within the cores, but will also increase the length of the cavity. The space between the magnets in the ring will therefore impose a constraint on the number of cores that may be used. The development of a cost model for the cavities will require consideration of the bias power supply, the high-power RF system and the low-level RF system as well as the estimated running cost. The MA cores are more complex to manufacture than the ferrite cores and may require a specific QA procedure to ensure that the cores will maintain their performance over the operational period of the facility. Deformation of

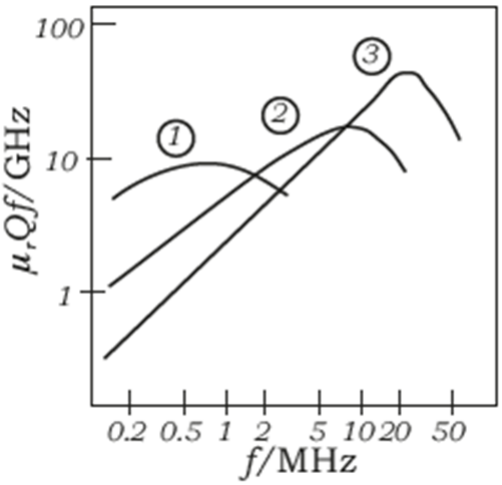

Figure 26: $\mu'_p Qf$ plotted as a function of frequency for three different types of ferrite material (1: Ferroxcube 4A, 2: Ferrox-cube 4C, 3: Ferroxcube 4E) [23].

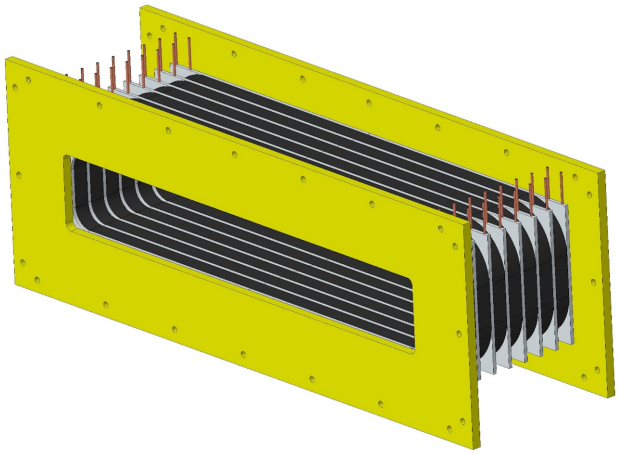

Figure 27: Schematic of the magnetic alloy core cavity.

Figure 28: A prototype core to be tested for the FETS FFA RF cavity.

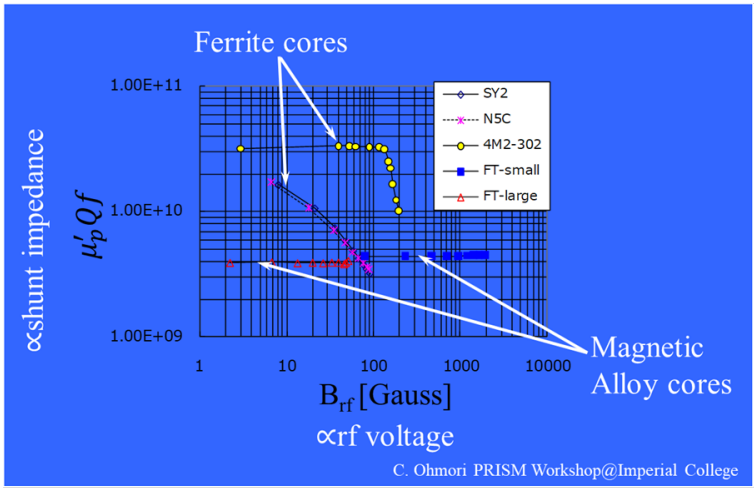

Figure 29: $\mu'_p Qf$ versus RF magnetic field for ferrite and MA cores.

Table 3: Parameters of the FFA magnet.

Parameter	Value
Number of cells	10
k range	4.37–5.55
dk/k (%)	< 1
Spiral angle (degrees)	48.7
r_0 (m)	3.477
B_0 (T)	1.405
Packing factor	0.34

the MA cores that have been observed in cavities operating at high power is not expected to be a problem due to the modest cavity gradient required for the LhARA FFA.

Plans

The principal goal for the present Preliminary Activity is to evaluate the degree to which each technology can meet the requirements of the LHARA FFA. To do this requires that the MA and ferrite material parameters are determined. Measurements of the material characteristics are being performed by ISIS Department personnel for the FETS FFA. These results can be used to evaluate the pros and cons of both the MA and the ferrite technologies for the LhARA FFA.

1.6.2 Magnet Design

The FFA ring consists of ten symmetric cells, each containing a single combined-function spiral magnet. The magnet parameters are given in table 3. The field index, k, is defined as:

$$k = \frac{r}{B_z}\frac{\partial B_z}{\partial r}\,; \tag{4}$$

where B_z is the vertical magnetic field and r is the radius measured from the centre of the ring. The FFA is required to deliver beams over a range of energies, each requiring a particular k-index to be provided by the

Table 4: Coil currents in the FFA preliminary design. The coil number corresponds to the ones labelled in figure 30. The power requirement (for this configuration is 16.5 kW per half magnet, or 33 kW total per dipole).

Coil Number	Length (m)	Ampere Turn	Power (W)
0	4.48	14227	2480
1	2.36	6220	2370
2	2.57	4220	1190
3	2.78	3416	841
4	2.98	2834	622
5	3.20	2411	483
6	3.41	2065	377
7	3.61	1774	295
8	3.82	1495	222
9	4.02	1183	146
10	2.75	6220	2760
11	2.96	4220	1370
12	3.16	3416	958
13	3.37	2834	703
14	3.58	2411	540
15	3.79	2065	420
16	4.00	1774	327
17	4.20	1495	244
18	4.41	1183	160

ring magnets. The integrated magnetic field on the median plane should follow the scaling law:

$$BL = BL_0 \left(\frac{r}{r_0} \right)^{k+1} ; \tag{5}$$

where:

$$BL = r \int B_z d\theta \, ; \text{and} \tag{6}$$

$$BL_0 = r_0 B_0 \Delta\theta \, ; \tag{7}$$

and $\Delta\theta$ is the opening angle of the magnet.

The scaling magnetic field is generated by having distributed conductors, a main coil, and 18 trim coils. A main coil wrapped around a flat pole generates the constant dipole field. The trim coils cross the pole face and return towards the outer radii of the pole. Powered with different currents, the trim coils generate the required field gradient. The details of the trim coils and an estimate of the total power required to deliver the currents can be found in table 4.

The configuration of the conductors can be found in figure 30. The trim coils are wrapped in two different vertical layers, with a "0.5-cell" offset between the two layers; this has been shown to improve the field quality by studies conducted for the FETS-FFA magnet, which has similar properties [24]. The main coil is labelled "0" and has a dimension of $75\,\mathrm{mm} \times 95\,\mathrm{mm}$ The trim coils are labelled from 1–18, each has dimensions of $10\,\mathrm{mm} \times 92.5\,\mathrm{mm}$.

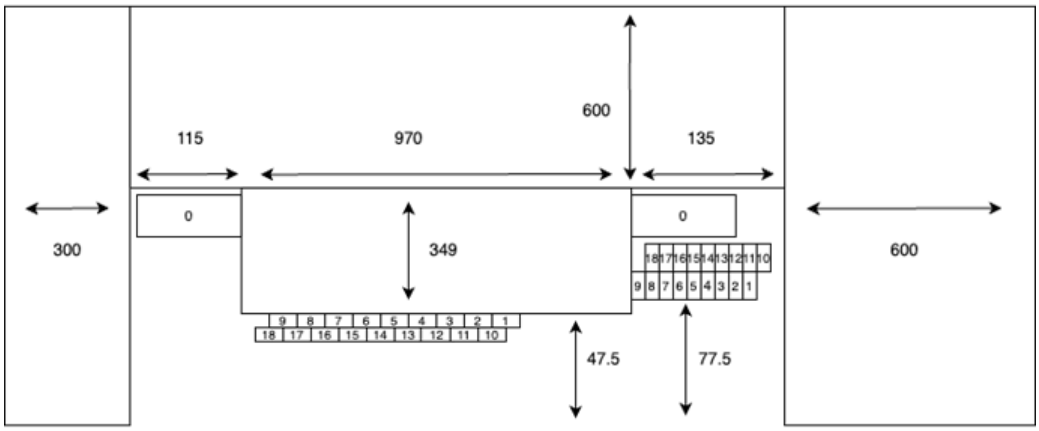

Figure 30: Schematic diagram of the cross section of the FFA magnet. The dimensions of the magnet are labelled in millimetres and the conductors are labelled from 0-18.

3D model

A 3D model was created in OPERA3D using the specifications given in table 3. The model was used successfully to compute the k-index, with a target value of $k = 5.33$. The result of the calculation is shown in figures 32 and 33.

The calculated k-index differs from that required by the scaling law by $\lesssim 1.5 \times 10^{-2}\%$. The requirement that $dk/k < 1\%$, is satisfied as the calculated k index lies within $\pm 0.6\%$ of $k = 5.33$ for all radii.

The field quality obtained from the OPERA3D model can be found in figure 31. The error on k lies within $\pm 1\%$, which satisfies the requirement defined in table 3. Field clamps will later be added to either side of the magnet to provide the following scaling conditions: fringe field extent scaling with radius; and constant spiral angle of the magnetic field.

1.6.3 FFA Injection Line

The LhARA Stage 2 FFA injection line begins at a switching dipole after Gabor lens 7 in the Stage 1 beam line. To inject on the inside of the FFA, the injection line crosses through the FFA ring between the magnets of two FFA cells. Modifications to the FFA ring from the original baseline design resulted in an increase of the orbit excursions, increasing the required magnet aperture. To ensure sufficient space, whilst also accommodating all infrastructure needs, including shielding, radiation shutters, vacuum pumps, diagnostics, and corrector magnets, poses engineering challenges in the design of the injection line crossing.

A new FFA injection line is proposed which includes two straight sections. The first straight section is 2.2 m long for the assumed 0.5 m thick concrete shielding, radiation shutter, and all other necessary devices. The second straight section is 1.85 m long to accommodate the FFA crossing. The number of quadrupoles required has increased from 10 to 11 but the physical dimensions of the quadrupoles are unchanged. The number of dipoles is unchanged, however two families of magnets are now required, one with a bending angle of 0.685 radians, the other 0.865 radians. All dipoles remain 0.7 m long. The switching dipole and injection septum magnets are unchanged. The total injection line length has increased from 14.6 m to 17.6 m. Figure 34 shows the layout of the new FFA injection line, rendered in BDSIM.

The initial conditions of the injection line in the baseline design assumed Twiss parameters of $\beta = 50$ m and $\alpha = 0$ in both transverse planes. When modelling beam transport in GPT in Stage 1, whilst considering space charge effects, both horizontal and vertical emittances are observed to grow from $\approx 8.6 \times 10^{-8}$ m rad to

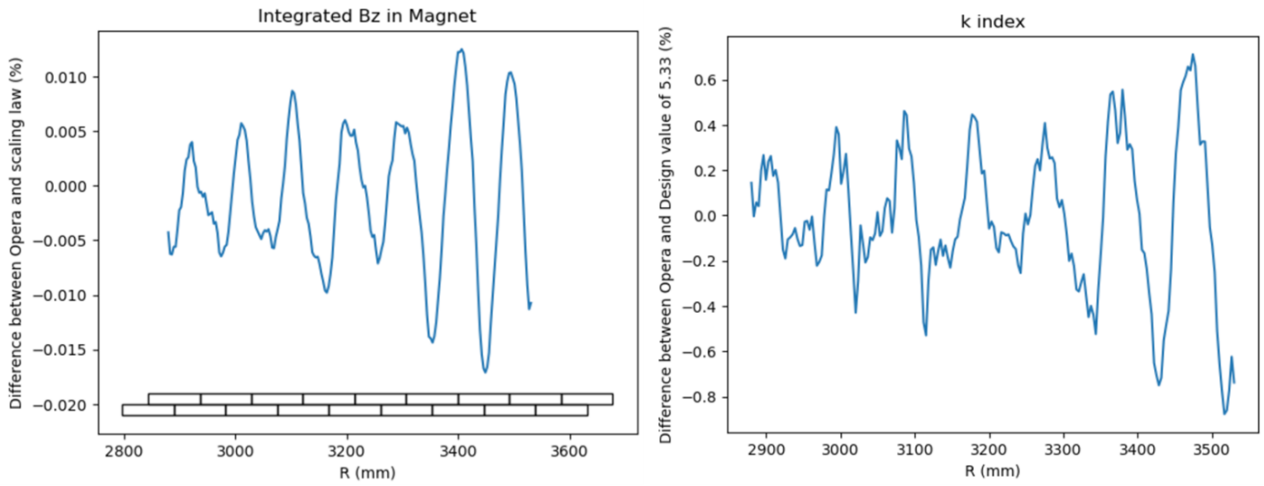

Figure 31: Field quality obtained from the OPERA3D model. (top) Difference between the integrated B_z in the model compared to the scaling law. The positions of the trim coils are shown at the bottom of the graph to compare the oscillation in the field quality to the structure of the trim coils. (bottom) Difference between the k-index – calculated from the B field obtained from the model – compared to the designed value of $k = 5.33$.

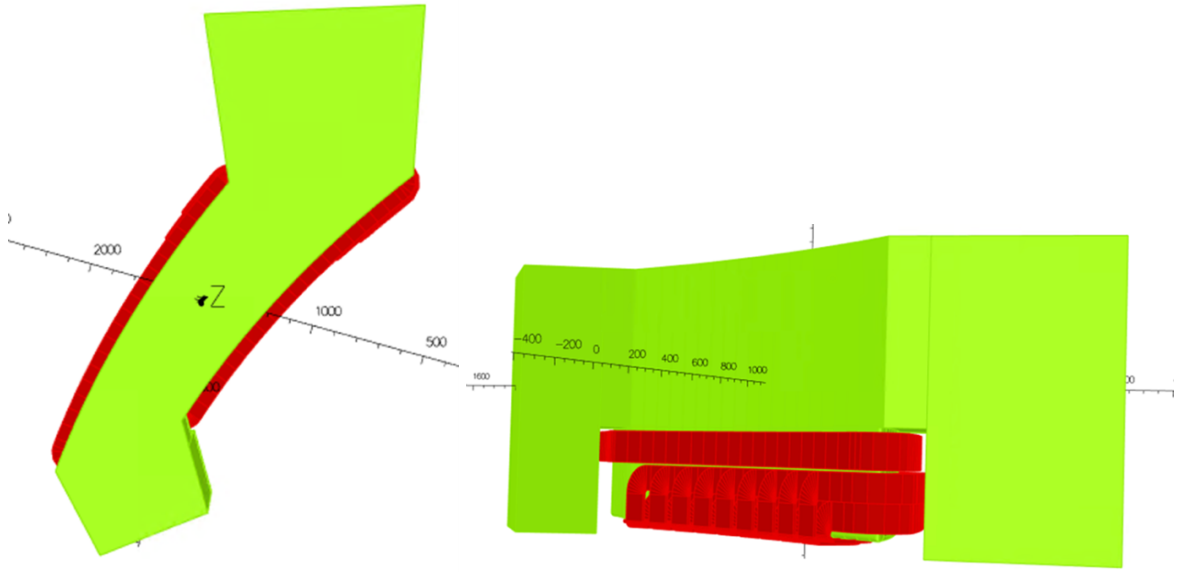

Figure 32: 3D model of the FFA magnet modelled in OPERA3D, only the top half of the magnet is shown. The conductors are shown in red with the iron in green. (top) View from above magnet (bottom) View of magnet from the side.

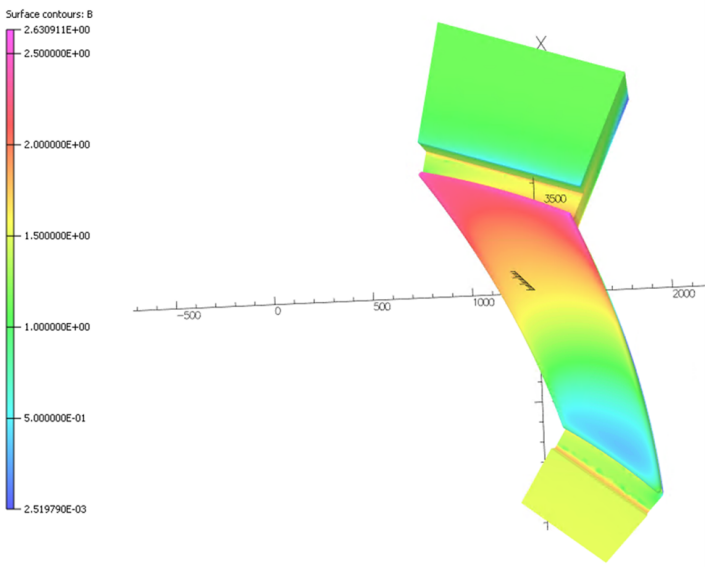

Figure 33: Magnetic flux density at the iron surfaces as calculated by OPERA3D. Fields can be seen to reach up to 2.6 T at larger radii, which is far into the saturation region; this will be addressed in later iterations of the design.

$\approx 3.5 \times 10^{-6}$ m rad. The initial beta value from the baseline design would result in a 1 sigma beam radius of 1.3 cm. The aperture of the switching dipole would therefore be larger than originally conceived, with a smaller aperture meaning that maintaining beam transport efficiency would be challenging.

To address this, the Gabor lenses in Stage 1 were re-optimized with GPT's optimization utility GDFSOLVE to reduce beta at the start of the switching dipole whilst preserving $\alpha_{x,y} = 0$. The normalised quadrupole strengths were varied with constraints of $|K1| \leq 17\,\mathrm{m}^{-2}$ so as to not exceed the maximum strength of any quadrupole in the baseline design. With the Twiss $\alpha_{x,y} = 0$ condition met, a solution with lower Twiss $\beta_{x,y}$ of ≈ 27 m was found. The proposed FFA injection line was subsequently re-optimised with this new initial beta value. The resulting horizontal and vertical beta functions and horizontal dispersion are shown in figure 35. The conditions at the end of the injection septum have been achieved whilst preserving the region of low beta and high dispersion. This low-beta, high-dispersion region is required for installation of a collimator to reduce the energy spread of the wide-band source emitted from the target down to the $\pm 2\%$ target for Stage 2 operating modes.

Engineering designs are currently being developed for the FFA ring and injection line. The perpendicular crossing angle, whilst providing sufficient space for beam transport, still causes geometric concerns regarding positioning injection line components in close proximity to the FFA magnets. Providing sufficient space for personnel to install and maintain the injection line also remains a concern, as the final magnets before the injection septum are too close to the FFA magnets. To address this, a preliminary design has been developed where the FFA crossing is at an angle with respect to the FFA aperture. This angle is chosen to be closer to the spiral angle of the FFA magnets, offering greater flexibility for positioning injection line components. The change of crossing angle consequently requires modifications to the bending angles of the injection line dipoles. A solution has been found that provides beam transport whilst also improving access between the line and FFA ring. Optics solutions have been found that match the FFA injection conditions, however there are concerns that a large beam radius at some locations may cause an unacceptable beam loss. Development of this alternative design continues.

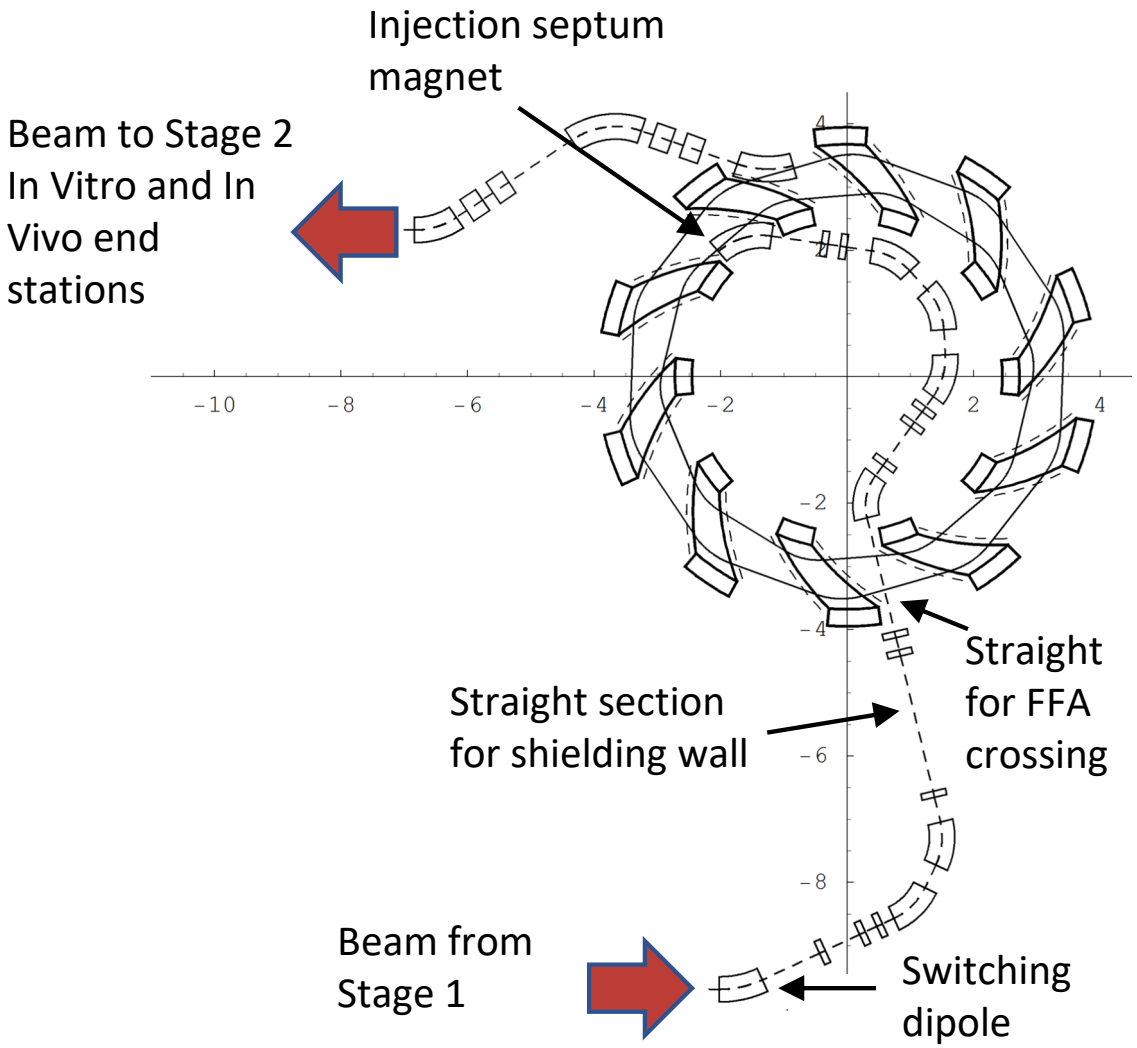

Figure 34: Layout of the Stage 2 FFA injection line.

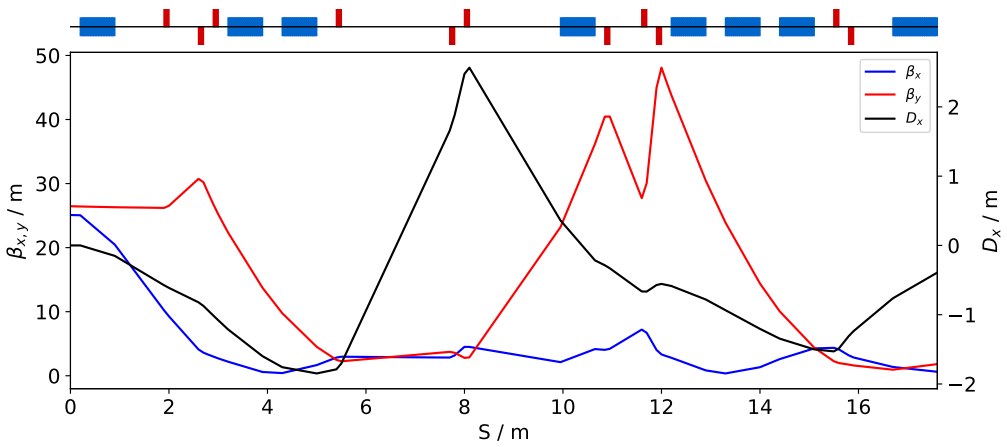

Figure 35: Horizontal and vertical Twiss beta functions and horizontal dispersion function of the Stage 2 FFA injection line.

1.6.4 Diagnostic System

The ITRF/LhARA facility will require several diagnostic systems. The use of a laser-driven ion source creates a beam with short bunches each containing a large instantaneous flux. The beam created at the target will have large peak current, very low emittance, high brightness, and very short bunch length, but a low average current. Emittance growth will occur as the beam propagates through the beamline and some beam loss is expected. In the absense of phase rotation, the bunch length will also increase, from almost 0 ns to the $\sim$ ns range in Stage 1, and to tens of ns in Stage 2. Here we discuss the diagnostics for commissioning and operation of the accelerator facility; the dedicated diagnostics systems for beam dose and quality measurements at the end stations are not covered.

Stage 1, injection line to FFA and HEBT

In Stage 1, the key parameters to be measured are beam size, beam position and beam current. The beam size and beam position can be measured with scintillating screens or Secondary Electron Emission (SEM) grids, each option will need to be retractable. The beam current can be measured non-destructively with Wall Current Monitors (WCMs), most likely passive devices due to the shortness of the bunch. A similar set of devices will be needed in the FFA injection and extraction lines, and in the high-energy beam transport (HEBT) line.

Precise measurement of bunch length may be challenging in Stage 1 due to a very short bunch length, this will require dedicated study. It may be possible to use WCMs in the extraction line and the HEBT as the bunch length will be longer.

It will also be necessary to measure beam loss. This can be performed with beam loss monitors based, for example, on plastic scintillators. Such monitors will be placed in the vicinity of the beam pipe in the areas where beam loss is expected.

FFA

The FFA will have special diagnostic requirements due to the complex shape of the vacuum chamber, see table 2. The key measurements for commissioning and operation of the FFA ring will be the beam trajectory (turn-by-turn position measurement), measurement of betatron tunes, and the beam current. The beam trajectory will be measured using capacitive pick-ups. A single pick-up device to measure both horizontal and vertical trajectory simultaneously is in development for the FETS-FFA project at RAL [25]. Measurement of the horizontal and vertical tunes can use the same capacitive pick-up device. However, the tune measurement will also require beam perturbation. A horizontal perturbation in the vicinity of the injection and extraction kickers can be excited using the kickers themselves. In order to measure horizontal tune on any orbit an RF knock-out method has been developed [26]. This technique exploits the horizontal dispersion so that when the beam receives a short acceleration burst from the RF cavity, it will start to oscillate. The vertical tune measurements will require a vertical exciter, which may be magnetic or electric. The measurement of betatron tunes may be made using the Base-Band Q (BBQ) technique with Direct Diode Detection [27], which allows the measurement of betatron tunes without any external excitation. However, this method has not yet been used in an FFA. Measurement of beam current will be performed using WCM with dimensions required by the FFA. This device should also allow the measurement of bunch length, and can be used to measure RF phase. Beam profile measurements may be performed using a wire scanner; beam loss can be measured in similar way to that proposed for Stage 1.

Status and future plans

All diagnostic devices discussed in the context of Stage 1 are based on established technology with the exception

of the bunch-length measurement which requires further study. The locations of the beam-profile monitors and WCMs for Stage 1 have been established. Work is underway to define the position of the diagnostics for the FFA injection line. FFA diagnostics have already been demonstrated at KURNS and development of diagnostics approprite for high-intensity beams is now progressing in the context of the FETS-FFA. Going forward, the LhARA project should develop further collaboration with the FETS-FFA project in the domain of diagnostics. Locations for diagnostics in FFA and for the HEBT remain to be studied.

1.6.5 Control and Feedback Systems

The ITRF/LhARA control system will be a facility wide monitoring and control system integrating all parts of the facility. The control system will extend from the interface of the equipment being controlled in the technical sub-systems through to the operator, engineering expert, physicist and end-station user. It will include all hardware and software between these bounds including computer systems, networking, hardware interfaces, programmable logic controllers (PLCs) and fieldbuses.

The Personnel Safety System (PSS) will be interfaced to, and monitored by, the control system. A separate event-synchronisation system will be implemented as part of the control system to ensure synchronisation of technical sub-systems and critical control operations and will also provide a common high resolution time-stamping and/or pulse-numbering capability.

The control system will benefit from existing control system equipment standards and knowledge gained from recently implemented ASTeC Radiation Test Facilities, e.g. CLARA. Consideration of technological advancement, e.g. new, more appropriate fieldbuses or protocols, will continue.

Architecture

The control system will be implemented using the `EPICS` software toolkit. `EPICS` is a proven software toolkit with well-defined interfaces at both the client and server and will enable fast integration and development. The choice of `EPICS` enables the project to take advantage of work done at other laboratories. `EPICS` has been successfully applied on previous projects at Daresbury including the ALICE, EMMA, VELA and CLARA facilities and on many accelerator projects worldwide. For previous Daresbury projects, extensive use has been made of `EPICS` Version 3 and more recently `EPICS` Version 7. For ITRF/LhARA it will be possible to deploy Version 7 and to use the advanced features exposed via the `pvAccess` protocol including manipulation and transport of structured data over the network.

The various components of the control system will be connected to a high speed Ethernet local area network. This will consist of several class C subnets connected to the main site network. Access will be provided to the control system data via `EPICS` gateway systems running access security.

The hardware interface layer of the control system will provide the connection to the underlying sub-systems. This will consist of a modular hardware solution of commercial rack mount PCs and embedded systems running the Linux operating system, real-time where required, connected to a range of I/O types directly or via selected field-buses.

Application software will be installed on central file servers to ensure consistent operation from any console on the control-system network. The control system will be implemented in such a way that it can be incrementally expanded and upgraded as the project proceeds. The control system must be able to be extended to new hardware and software technology, A number of `EPICS` client interfaces will be supported for controls and user application development in high-level languages. This is likely to include both Channel Access and `pvAccess` interfaces for languages such as `C#/VB` via `.NET`, `Matlab`, `Mathematica` and `Python`.

Controls hardware

The network hardware and commercial PC hardware of the control system will use standards defined by the

STFC Digital Infrastructure department. As far as possible controls hardware used on recent ASTeC Radiation Test Facilities should be preferred to take advantage of existing expertise and proven hardware standards. This hardware includes:

- *Industrial rack mount PC systems running a Linux operating system, with potential for a real-time kernel, as required*: Existing `EPICS` support is available for interfacing many I/O types including analogue, digital and serial (RS232/422/485) along with status/interlocking via Ethernet-connected Programmable Logic Controllers.
- *Omron NJ series PLCs*: Status and interlock systems for digital control and machine protection of accelerator hardware and sub-systems. As a replacement for Omron CJ series PLCs deployed on previous ASTeC RTFs, the NJ PLCs will either be integrated directly into the `EPICS` control system utilising the CIP protocol, or indirectly via a data aggregation tool with EPICS integration via OPC-UA or similar. This will allow PLC data tags to be directly mapped to `EPICS` process variables and/or to `pvAccess` structured data types.
- *Motion control systems*: Fieldbus based systems with remote I/O via EtherCAT. In common with CLARA and building on this experience, these will comprise of Beckhoff TwinCAT real-time controllers with EtherCAT connected motion control and I/O modules. These controllers interface with the `EPICS` control system via Modbus TCP.

Any specialist control requirements will be addressed using dedicated real-time controllers (for example embedded industrial hardware or FPGA based). Examples of such systems could include geographically isolated devices or systems that require the computing speed of a dedicated CPU. Any dedicated controllers would be integrated into the `EPICS environment` and software-build processes.

Due to the pulsed nature of the facility, dedicated real-time systems will be required. Likely applications include data acquisition for beam diagnostic measurements or RF system measurements. For previous ASTeC RTF control systems VMEbus processors and FPGA based I/O carriers have been used. It is expected that the modular, open standard, MicroTCA protocol will be adopted as a replacement for VMEbus. Options for embedded MicroTCA controllers and FPGA carriers will be evaluated further in the Technical Design phase.

Virtualisation

Virtualisation technology will be used both in the server infrastructure layer and, where appropriate, in the EPICS input/output controllers. This will increase flexibility, scalability, reliability and efficiency of the control system by abstracting hardware specifics from the controls software.

Timing and synchronisation system

One of the principle challenges with a network-distributed control system is the synchronisation and accurate time-stamping or pulse numbering of events spread across several physically and logically separated systems. An example of this is the simultaneous measurement of beam diagnostic information along an entire beam transport system. This operation will typically involve collecting beam-synchronous data simultaneously from a number of front-end server systems. Commercially available synchronisation hardware, as used on CLARA, is available for a number of platforms and provides timing outputs for ITRF/LhARA applications. It will be important to ensure that the master clock used by the timing system is locked to the RF and laser systems. GPS atomic clock synchronisation will be used to distribute accurate time-stamp via the timing system and can also be used to discipline the RF master oscillator.

Interlock systems

The control system will provide a comprehensive interlock and machine protection system ranging from the enforcement of sensible operating limits right through to the protection of the facility against potentially dan-

gerous operating conditions. The interlock system may be defined using two classes of system:

High Integrity: If and where required, this will be used to provide high-speed and fail-safe local protection in situations where serious damage to equipment is likely to occur. Embedded micro-controllers could be used for this purpose.

Routine: This level of protection is intended to prevent minor damage to individual machine components or sub-systems. An Omron PLC based interlock system based on experience of other facilities will be used for this purpose.

Both interlock systems will operate independently of EPICS with monitoring and control requests marshalled to the interlock systems via EPICS for processing via internally programmed logic. In addition, but not described here, there will also be local systems that supervise individual components such as RF structures. Personnel safety musy be ensured using a:

Personnel Safety System: This section does not cover details of the protection of personnel from facility hazards. In terms of logic implementation, the PSS would be implemented using Omron safety controllers. The NX controllers make use of Ethernet based safety protocols and are more suited to a new facility, easing installation and enabling greater scalability and flexibility. Full monitoring of the PSS will be provided through the control system.

Feedback systems

Digital feedback will be required in a number of places. The primary requirements include closed-loop control of amplitude/phase in RF systems, and water cooling for high-power RF infrastructure and accelerating cavities.

Slow feedback and control, e.g. for water temperature stabilisation, can either be implemented in the commercially supplied system, or within the control system via PLC or EPICS PID control. Ideally, the use of commercial systems should be limited to those that support integration into the control system to allow remote monitoring and control.

For faster, lower-latency feedback control, direct integration into the control system is required. RF amplitude/phase control, will be achieved either by embedding the control directly into the FPGA of the LLRF controller or using dedicated software directly on the CPU of the LLRF controller. Options for embedded feedback control will be evaluated further in the Technical Design phase.

High-level application software

During operation, high-level applications are required that will communicate via the control system. A mid-level interface is required to abstract away the detailed implementation of devices in the control system. This will allow operators and users to interact with sub-systems and devices in a consistent, structured and well-defined way. Options developed and used previously include common C++/Python mid-level interfaces to the control system, CATAP: 'Controls Abstraction To Accelerator Physics'. Also pvAccess interface using EPICS Version 7 to represent sub-systems and devices as consistent, structured data for direct consumption by high-level application software.

1.6.6 ITRF/LhARA Building Concept Design

Referring to [1] (page 54), the building concept design is well described and has not changed significantly since the 12-month report was published. Work is progressing in the region of the FFA ring and the building size requirements will need to be reviewed when the position and size of the ring has been more fully determined.

Table 5: Source terms defined for the ITRF/LhARA project.

	Mode	1	2	3	4	5	6
A0	Plasma source	98	98	98	98	98	98
A	Source nozzle	30	33	30	30	30	30
B	Collimator	25	25	25	25	25	25
C	Source shutter	0	0	**100**	0	0	0
D	In-vitro Stage 1 delivery (arc collimator)	25	0	0	25	0	0
E	In-vitro Stage 1 station	**100**	0		**100**	0	0
F	Injection line (Stage 1 shutter)	0	25		0	25	25
G	FFA acceleration		10			50	10
H	FFA extraction		10			10	10
I	FFA beam dump		0			**100**	0
J	FFA shutter		0			0	0
K	In-vitro Stage 2 delivery		0 or 25				0 or 25
L	In-vitro Stage 2 station		**0 or 100**				**0 or 100**
M	Stage 2 shutter		0				0
N	In-vivo delivery		**0 or 100**				**0 or 100**

1.6.7 Bulk Shielding Assessment

Consolidation of source terms

The output of a shielding assessment is entirely dependent on the source terms that are provided to the calculation. A meeting held at Daresbury Laboratory on 1st November 2023 – involving physicists from partner institutions, relevant STFC staff and an external shielding assessor – focused the attention of the various stakeholders on the issue of the source description. This proved to be instrumental in explaining what source-term format was required to enable the shielding calculations and laid the foundations for the functional source-term data sheet currently being used to perform the bulk shielding assessment.

The data sheet consists of a schematic of the facility, displaying each significant source, i.e. each location where a substantial proportion of the proton beam is lost, such as the collimators, the shutters and the beam dumps. The beam loss statistics for each source in each mode are outlined in table 5 (grey shading denotes the termination of the beam), noting that for Modes 2 and 6, the beam either ends at the *in-vitro* or *in-vivo* end stations and not both simultaneously.

In addition, the initial plasma source term has been simulated and all key parameters such as the beam energy distribution, divergence, initial proton/ion yield have been derived from this. Combining this plasma source with the loss points, each mode of operation has now been described in terms of which source points are engaged and what the particle loss rate is at that point. The source term also contains the operating schedule; the temporal parameters, such as the availability of the machine and the expected duration of "beam on" time and which fraction of this is attributed to each operational mode. The latter are necessary to understand the accumulated exposure and residual activation of components.

As of the date of this report, the final source description is only missing the initial electron component from the stripping of the protons at the very start of the process. Aside from that, the source term is complete for use in shielding calculations; table 6 below summarises the nominal, bounding source term for each stage of normal operation.

Table 6: Nominal and bounding source terms.

	Stage 1 operation		Stage 2 operation	
	Protons	C^{6+} ions	Protons	C^{6+} ions
Max beam energy (MeV)	15 MeV	48 MeV	127 MeV	400 MeV
Repetition rate (Hz)	100	100	100	100
Particles required at delivery point (#/s)	1×10^{10}	1×10^{9}	1×10^{10}	1×10^{9}

Engagement of shielding assessors

The source-term meeting held on 1st November 2023 introduced TUV-SUD's dedicated shielding assessment team to the project. Expert guidance was provided in the initial meeting to ensure a suitable source term was described and their services are now fully engaged to provide the bulk shielding assessment to which this milestone relates.

A contract of work, split into two phases was partially approved, with Phase 1 work (shielding design basis and bulk shielding assessment) to be delivered next financial year (24/25) and Phase 2 work (fault scenarios, material activation and residual dose rate assessment) to be delivered at a later date. The anticipated availability and duty cycle of the facility may give rise to significant residual activation, which may overtake the external dose rates as the limiting factor in these radiation assessments.

As of the date of this report, the shielding design basis is at around 70% completion; final edits and a quality assurance check are required. This is the key document that establishes the standards, source and material data, radiological design criteria and layout with approach to designation of areas which will be used for all facility radiation shielding calculations. This allows a consistent approach to all shielding calculations, even between different shielding assessors and formalises any assumptions made in a transparent document. The designation of radiological areas methodology is also determined within the shielding design, containing projected area designations through the entirety of commissioning and normal operation phases.

From this shielding design basis, TUV-SUD have now begun work on the bulk shielding assessment, with an estimated completion date in May/June 2024.

Next steps

In the upcoming financial year, the bulk shielding assessment for the facility will be delivered and interpreted, allowing it to feed into future operational and design decisions.

1.6.8 Mechanical Systems Integration Support Concepts

Support systems for accelerator devices are required to be stable, minimise effects due to vibration and include adjustment to facilitate accurate positioning of equipment. The support concepts adopted by ITRF/LhARA have been developed and successfully implemented on other accelerator projects such as CLARA and ESS. The concept adopts a modular system which facilitates assembly and offline testing of accelerator equipment before installation into the accelerator hall enabling the most efficient use of time particularly during critical shutdown periods.

Ti:S Laser support system

It is envisaged that the Ti:Sapphire laser system will be procured and supplied by a specialist commercial company; the supports for this system will be included during the scope of design and procurement.

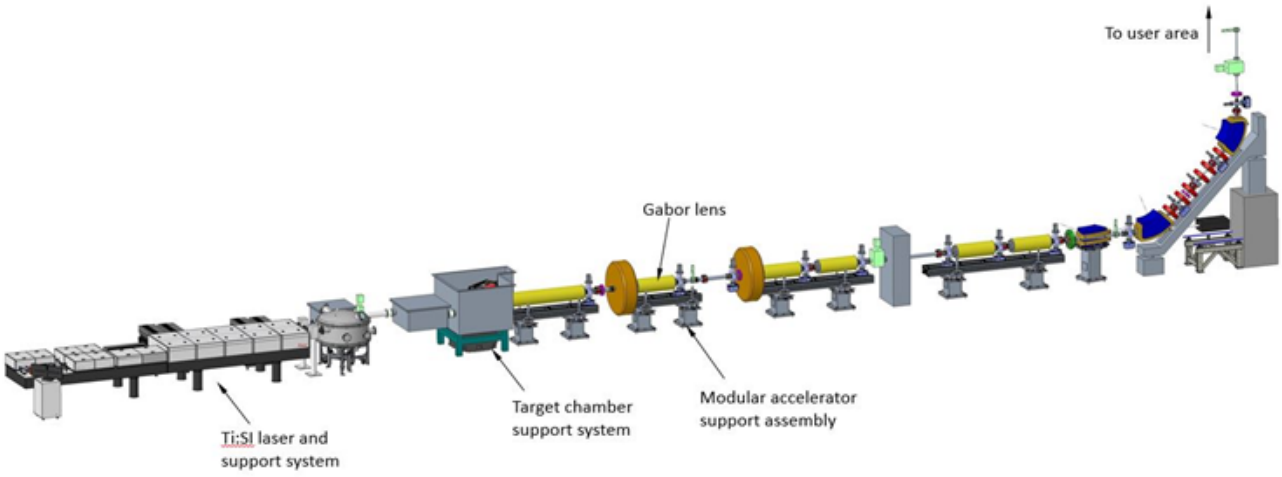

Figure 36: Stage 1 layout.

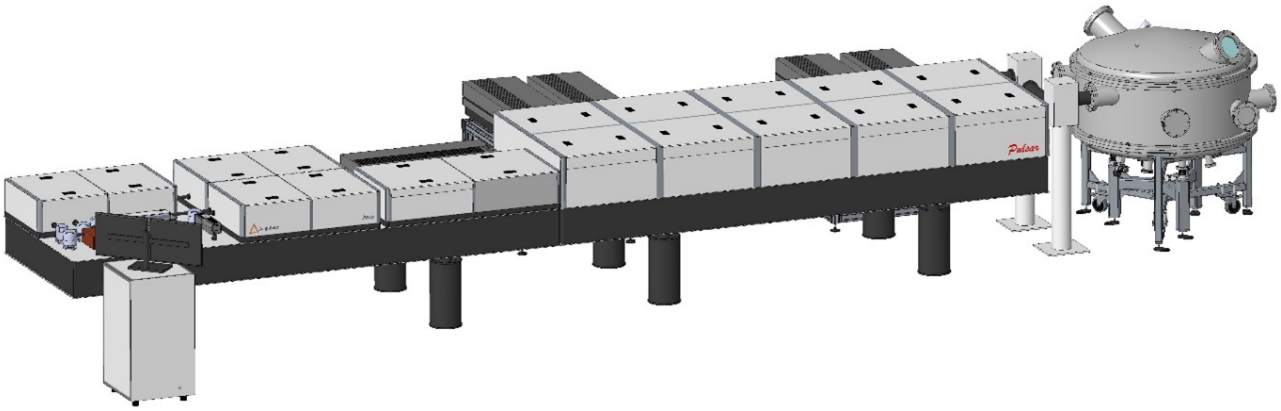

Figure 37: Laser layout.

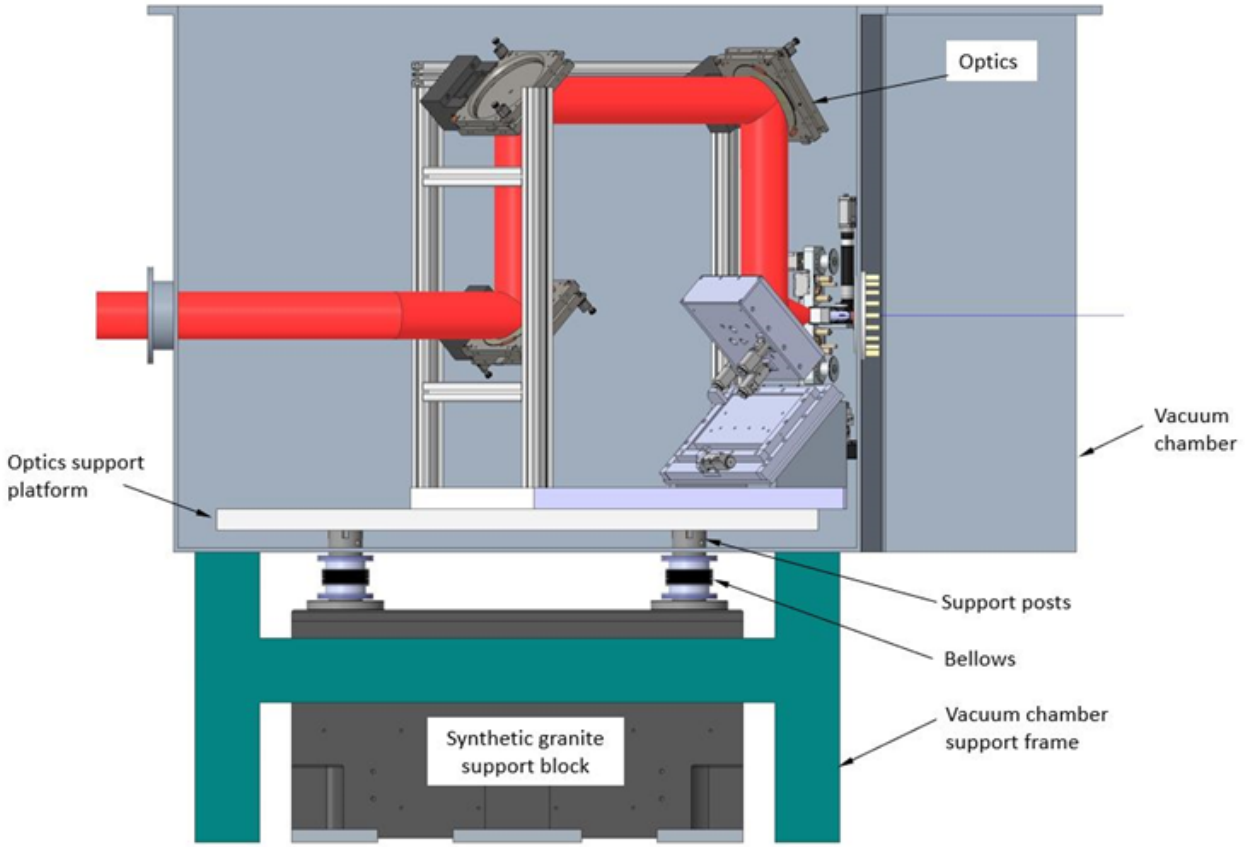

Figure 38: Source layout.

Laser target optics support system

For optical support systems, such as the laser target chamber source, it is critical that the optical element supports are isolated from the vacuum chamber which will deflect during pump down. In figure 38 optics are shown mounted onto a baseplate which is isolated from the vacuum chamber with bellows and supported by a synthetic granite block for vibration damping. The vacuum chamber is supported by an independent frame with adjustments available in X, Y and Z.

Accelerator support systems

Each modular support system includes two pedestals and an aluminium extruded beam as shown in figure 39. The support pedestals are fabricated in mild steel and consist of a thick wall support tube with a top and bottom plate. The beam assembly is constructed from rectangular aluminium extrusion which includes flat surfaces with tolerance specification, T-slot features for clamping equipment and ancillary equipment such as electrical and water services. The beam assembly is supported by the pedestals utilising a three-point kinematic system allowing for adjustment in direction Y and also pitch, roll and yaw. Adjustment of the beam in directions X and Z is achieved by translation of a plate using screws.

Accelerator equipment and devices that are assembled to the support beam have independent kinematic support and adjustment providing translation in X, Y and Z together with pitch roll and yaw. Figure 40 shows examples of a quadrupole and corrector magnet assembled to a support beam. All accelerator devices will have features for inserting laser-tracker-survey fiducials to enable pre-alignment of each module.

The Gabor lens support features have not been determined at this stage. However, it is envisaged that the proposed modular support beam system would be an appropriate concept as shown in figure 41.

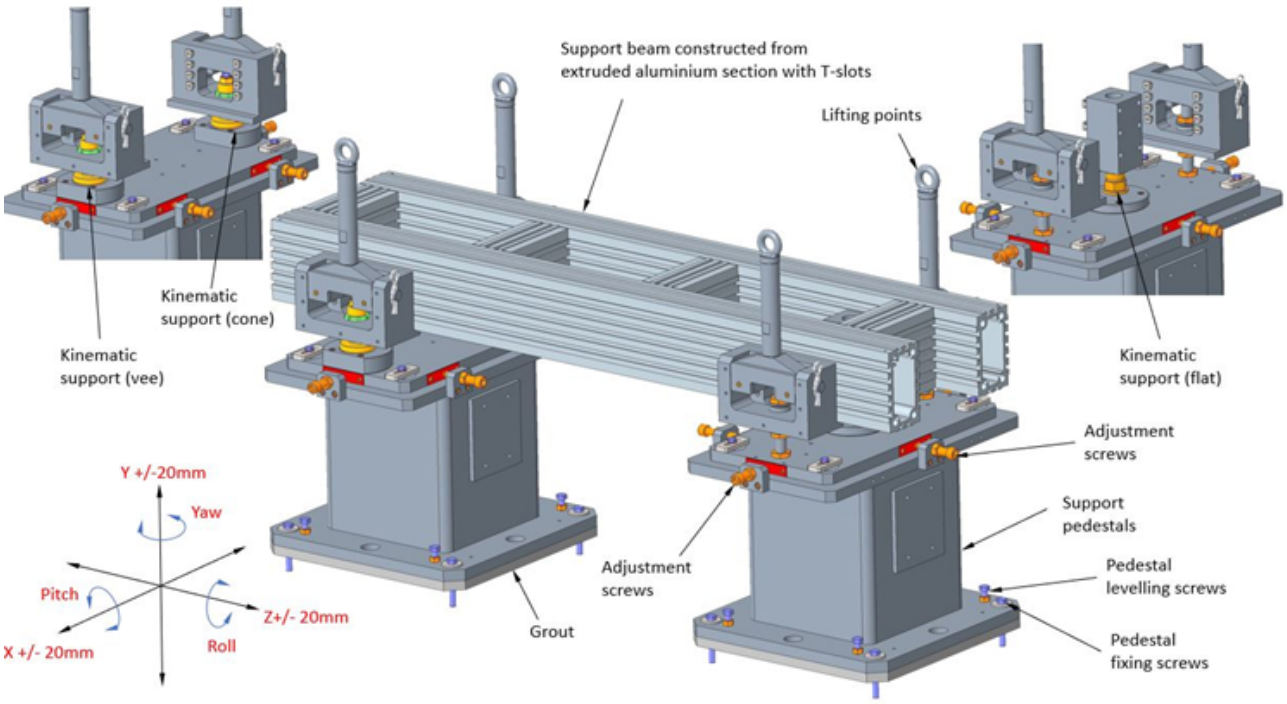

Figure 39: Support systems.

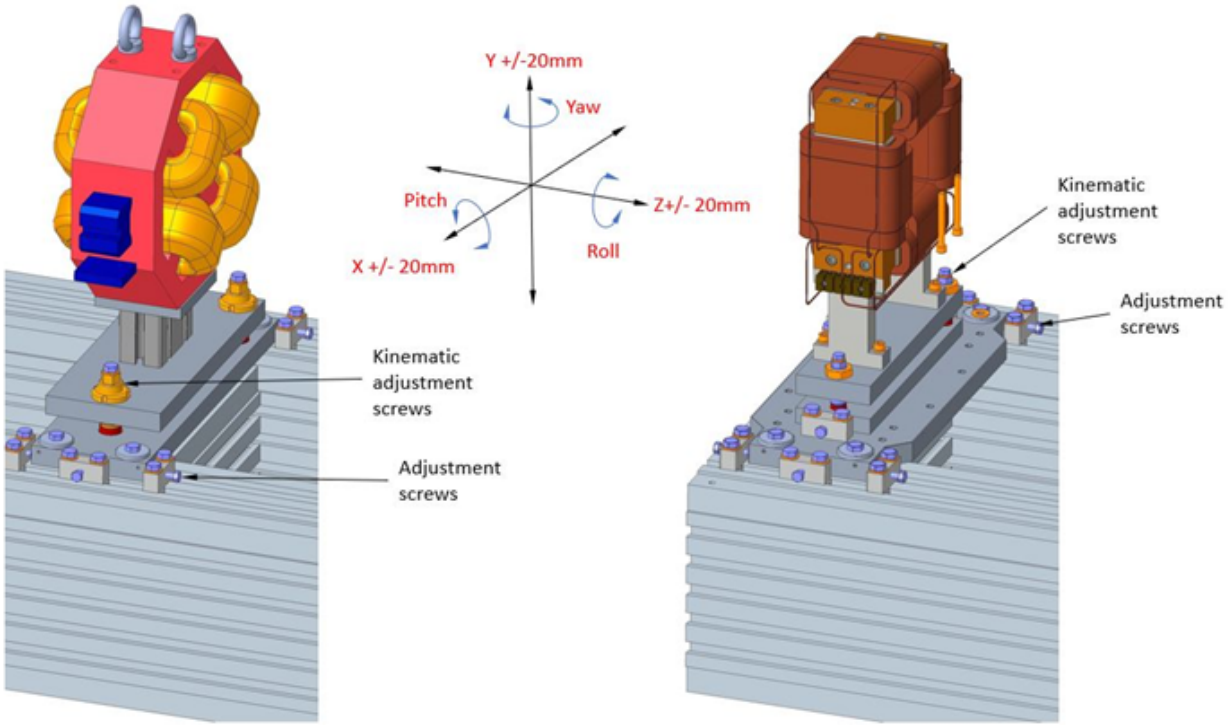

Figure 40: Kinematic mounts.

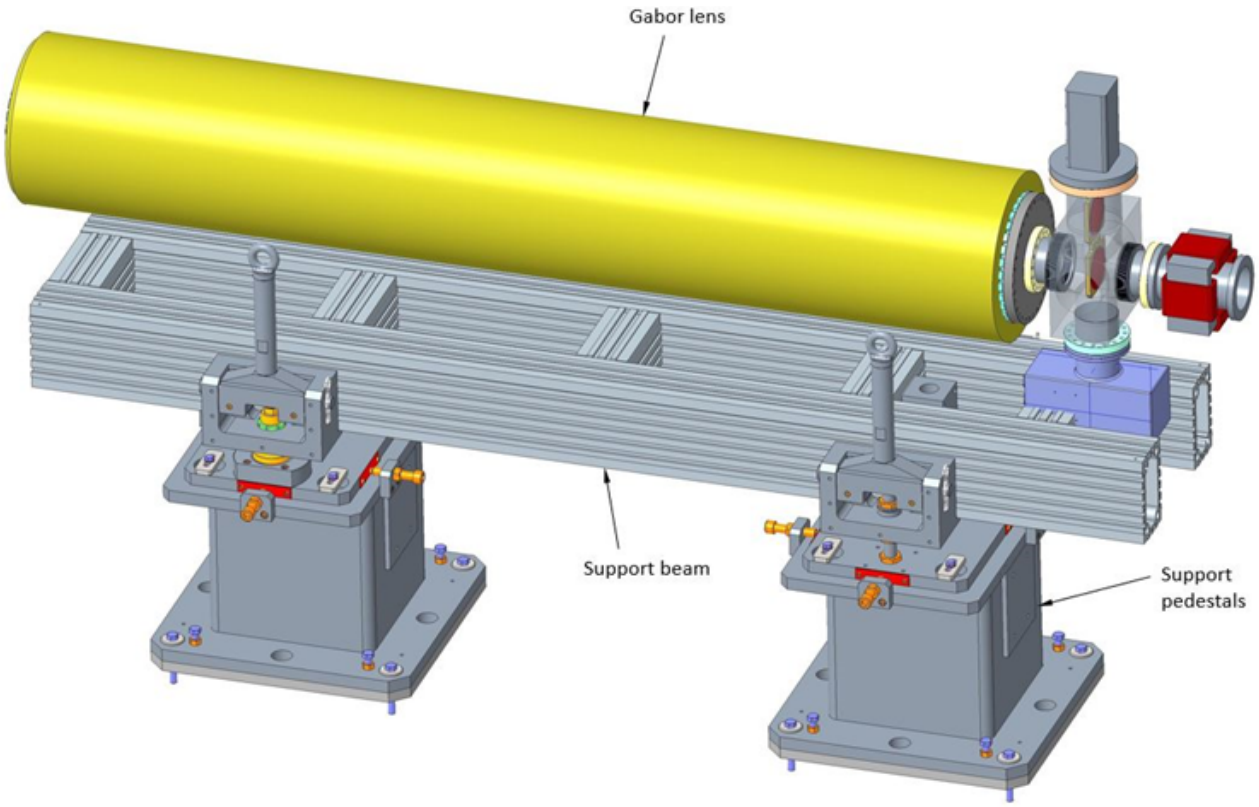

Figure 41: Gabor lens support system.

Building offline in a modular way also enables the installation of local services allowing for testing of systems such as vacuum integrity, magnet power and water cooling systems. Following offline testing the beam assembly module can be transported to the accelerator hall using a lifting beam and attachments. The support pedestals are installed with the bottom plate set 25 mm above the floor, and after levelling, are secured with bolts; a high-strength grout is applied in the gap under the pedestal plate. The pedestals are filled with dry sand to act as a vibration damper and minimise any effects on the devices. The aluminium beam assembly is located using the three-point kinematic support system and secured with fasteners.

Alignment of the beam assembly is achieved by using the adjustment features described above and with a laser tacker which accurately reads back the position of fiducials placed into holes in the corners of the beam assembly.

Equipment required for transporting the beam vertically to the user areas it is envisaged that the same modular system. A concrete block can be used to elevate the support pedestal at one end as shown in figure 42.

1.6.9 Vacuum Concepts

The vacuum system of the will require several different vacuum regions with a variety of operational requirements and different specifications. The first key area is the target chamber where ions are produced and there is a significant gas load. This is then directly coupled into the low-energy beamline with Gabor lenses, where performance needs to be optimised to avoid degrading the beam properties. The high-energy line requires a similar level of vacuum to the low-energy line, whereas the fixed-field accelerator, due to particles recirculating, will require a higher vacuum. The laser system will have a vacuum requirement to maintain beam quality and reduce scattering. The make-up of the end stations is currently unknown but may require vacuum. Finally, RF

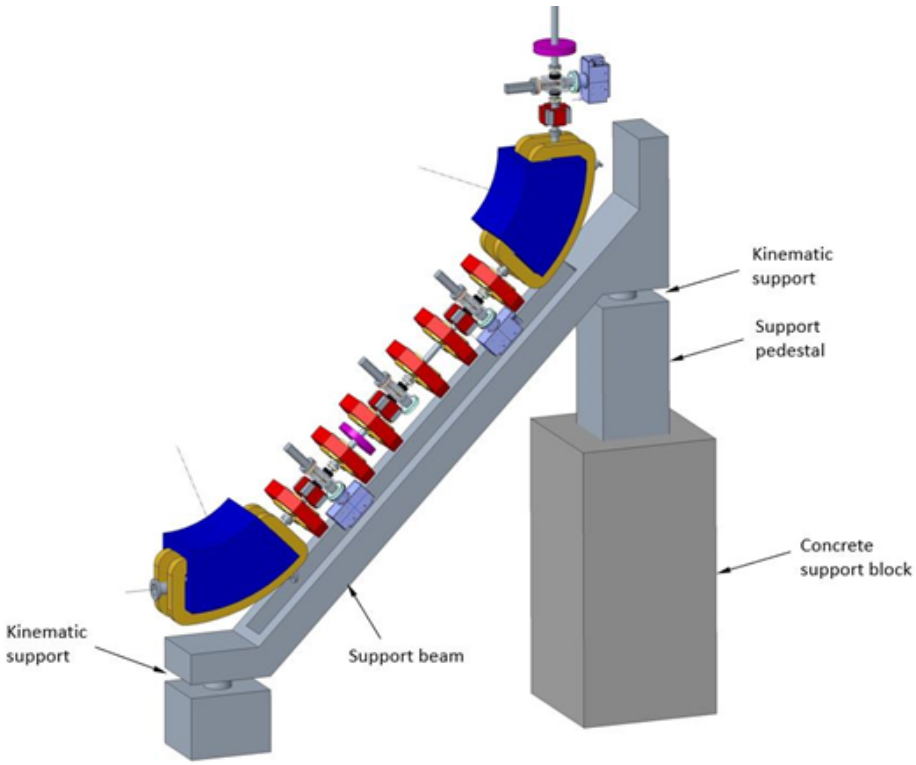

Figure 42: Stage 1 arc.

waveguides may be needed where a vacuum system should be used over the more conventional SF_6 gas-filled waveguides because of the negative environmental impact of SF_6.

The currently assumed vacuum levels are presented in table 7 and based on accelerator-design experience. These values need to be confirmed by simulating the effect of residual gas on beam propagation. Vacuum modelling will then be required to ascertain where vacuum pumps should be placed.

The vacuum system requirements falls comfortably in the ultra-high vacuum region and therefore the general design principles for this vacuum regime will be adopted. The Vacuum Quality Assurance Documents developed at Daresbury Laboratory, for modern accelerator applications, provide a good example of design principles that can be adopted.

Vacuum technology

In general, the vacuum system design is based on well-tried and well understood design principles. The machine will be split into vacuum regions separated by gate valves for practical reasons and for machine protection. Dividing the machine into discrete vacuum regions makes it easier to install and commission whilst at the same time simplifying maintenance and breakdown interventions. In most circumstances gate valves will be all-metal. Roughing valves (right angled valves) and let up valves will be located in each vacuum region. ConFlat(TM) Flange (CF) will be used as the most common type of flange connection for ultra-high vacuum systems and uses the knife-edge principle to achieve an all-metal vacuum seal.

All vacuum components will undergo a full UHV cleaning procedure followed by a vacuum bake to 250°C for 24 hours before installation (ex-situ) where possible. This will reduce contaminants and surface outgassing enabling the design pressure to be reached. The beam line is approximately 80 m in length with a number of chambers for screen diagnostics and 7 Gabor lenses. Predominately, this needs to be held at a base pressure of 1×10^{-8} mbar. The number of 100 l/s ion pumps required to achieve a base pressure of 9×10^{-9} is calculated

Table 7: Mean working pressures assumed for each vacuum region.

Subsystem	Mean working pressure (mbar)
Laser systems	TBC
Laser beam Conditioning chamber	TBC
Target chamber	1×10^{-6}
Gabor lenses	1×10^{-8}
Low energy line	1×10^{-8}
Low energy in vitro end station	TBC
Fixed Field Accelerator	1×10^{-9}
High energy line	1×10^{-9}
High energy in vitro end station	TBC
High energy in vivo end station	TBC

using the vessel surface area and relevant outgassing figures. For a stainless-steel vessel 80 m in length and 38 mm in diameter with 18 screen chambers, UHV cleaned and baked ex-situ, a minimum of 31 ion pumps are required.

Additional pumping speed will be required for the larger surface area of the Gabor lenses, where we may use a higher-capacity pump to achieve the vacuum level required or increase the number of pumps in this area.

Vacuum will be achieved using pumping carts, a combination of turbo-molecular pumps backed by scroll pumps, to remove gas quickly from the section. Ion pumps with optional NEG (non-evaporable getter) cartridges will then be used for maintaining vacuum during normal operations. The ion pumps have the advantage of being static and so do not introduce any vibrations into the system. NEG cartridge pumps once activated have the ability to pump without electrical power and may be a useful addition to reduce energy demand. The laser transport lines, target chamber and differential pumping will use turbo-molecular pumps backed by scroll pumps to achieve the desired working pressures.

The vacuum system will be equipped with the relevant diagnostic instrumentation in each section, vacuum gauges (Pirani and Inverted Magnetron) and residual gas analysis. This allows the environment to be monitored, analysed and problem solving to be carried out when required. The vacuum system will be linked into the controls system for monitoring and to enable machine protection. Interlocks between sections will be used to prevent accidental venting of the machine or catastrophic failure, these will be driven by the diagnostic instrumentation.

The control system should also be enabled with a 'standby' mode allowing the controlled reduction of running pumps and controllers. In conjunction with NEG this allows the electrical power demand to be reduced impacting the CO2 production and running costs.

Modelling

As usual, a number of iterations of machine layout and calculation of pressure distributions will be required before a satisfactory final scheme of vacuum pumping can be determined in the TDR stage. Two areas have been highlighted as challenging from a vacuum perspective and require further investigation to understand if the concept works.

The first is the vacuum connection of the target chamber to the low energy beam line due to different operating pressures of 10^{-8} mbar and 10^{-6} mbar. The calculation of the conductance of the nozzle between the two will give an understanding of the impact on the vacuum from connecting these two volumes. The nozzle diameter can be optimised between ion beam diameter requirements and vacuum specification. The gas produced from

the film target and its trajectory is unknown and could have an impact on the overall design due to the beaming effect.

The second challenge is the ability to pump the first Gabor lens as there is a requirement to site the lens as close to the ion source as possible, leaving little room for a vacuum pump. As the target is a gas source, we will have a higher pressure at one end of the Gabor lens than the other. This may be detrimental to the operation of the lens. Modelling needs to be done to understand the pressure profile in this area. The mechanical design needs to be further understood in this area to enable the inclusion of pumping ports to achieve the Gabor lens operating pressure.

1.6.10 Power consumption and cooling requirements

Referring to [1] (pages 73–76) the power consumption and cooling requirements are well described and have not changed significantly since the report was published. Work is progressing in the region of the FFA combined function magnet; the power and water cooling requirements will need to be reviewed when the magnet design has been determined.

References

[1] **LhARA** Collaboration, C. Baker *et al.*, "LhARA/ITRF: twelve month progress report," Tech. Rep. LhARA-Gov-PMB-2023-06, 2023. https://ccap.hep.ph.ic.ac.uk/trac/raw-attachment/wiki/Research/LhARA/Documents/LhARA-Gov-PMB-2023-06-Final.pdf.

[2] G. Aymar, T. Becker, *et al.*, "LhARA: The Laser-hybrid Accelerator for Radiobiological Applications," *Frontiers in Physics* **8** (2020) . https://www.frontiersin.org/articles/10.3389/fphy.2020.567738.

[3] The LhARA consortium, "The Laser-hybrid Accelerator for Radiobiological Applications," Tech. Rep. CCAP-TN-01, The Centre for the Clinical Application of Particles, Imperial College London, 2020. https://ccap.hep.ph.ic.ac.uk/trac/raw-attachment/wiki/Communication/Notes/CCAP-TN-01.pdf.

[4] "ITRF 6-Month Report," hrefhttps://stfc365.sharepoint.com/sites/ITRF/Shared Documents/Forms/AllItems.aspx2023.

[5] **LhARA** Collaboration, "LhARA Project Management Board pages," https://ccap.hep.ph.ic.ac.uk/trac/wiki/Research/LhARA/Governance/ProjectManagementBoard, 2023. Accessed: 2023-03-21.

[6] **LhARA** Collaboration, "Laser-driven proton and ion source," https://ccap.hep.ph.ic.ac.uk/trac/wiki/Research/LhARA/LaserDrivenSource, 2023. Accessed: 2023-03-21.

[7] **LhARA** Collaboration, "Gabor Lens," https://ccap.hep.ph.ic.ac.uk/trac/wiki/Research/LhARA/GaborLens, 2023. Accessed: 2023-03-21.

[8] **LhARA** Collaboration, "Ionacoustic dose mapping," https://ccap.hep.ph.ic.ac.uk/trac/wiki/Research/LhARA/IonAcoustic, 2023. Accessed: 2023-03-21.

[9] **LhARA** Collaboration, "End station R&D and vertical beam line development," https://ccap.hep.ph.ic.ac.uk/trac/wiki/Research/LhARA/EndStation, 2023. Accessed: 2023-03-21.

[10] **LhARA** Collaboration, "Accelerator design and facility integration," https://ccap.hep.ph.ic.ac.uk/trac/wiki/Research/LhARA/DesignAndIntegration, 2023. Accessed: 2023-03-21.

[11] **LhARA** Collaboration, "LhARA Executive Board," https://ccap.hep.ph.ic.ac.uk/trac/wiki/Research/LhARA/Governance/ExecutiveBoard, 2023. Accessed: 2024-06.

[12] The LhARA collaboration, "Baseline for the LhARA design update," Tech. Rep. CCAP-TN-11, The Centre for the Clinical Application of Particles, Imperial College London, 2022. https://ccap.hep.ph.ic.ac.uk/trac/raw-attachment/wiki/Communication/Notes/CCAP-TN-11-LhARA-Design-Baseline.pdf.

[13] **LhARA** Collaboration, "NOVEL END-STATION DEVELOPMENT: CONSULTATION 1," https://indico.stfc.ac.uk/event/668/, 2022. Accessed: 2023-09-30.

[14] **LhARA** Collaboration, "NOVEL END-STATION DEVELOPMENT: CONSULTATION 2," https://indico.stfc.ac.uk/event/780/, 2023. Accessed: 2023-09-30.

[15] **LhARA** Collaboration, "LhARA Collaboration Meeting," https://indico.stfc.ac.uk/event/986/, 2024. Accessed: 2024-06.

[16] X.-P. Huang, F. Anderegg, E. M. Hollmann, C. F. Driscoll, and T. M. O'Neil, "Steady-State Confinement of Non-neutral Plasmas by Rotating Electric Fields," *Phys. Rev. Lett.* **78** (Feb, 1997) 875–878. https://link.aps.org/doi/10.1103/PhysRevLett.78.875.

[17] "Geant4," https://geant4.web.cern.ch/.

[18] J. Allison, K. Amako, *et al.*, "Geant4 developments and applications," *IEEE Transactions on Nuclear Science* **53** no. 1, (2006) 270–278.

[19] J. Allison, K. Amako, *et al.*, "Recent developments in Geant4," *Nuclear Instruments and Methods in Physics Research Section A: Accelerators, Spectrometers, Detectors and Associated Equipment* **835** (2016) 186–225. https://www.sciencedirect.com/science/article/pii/S0168900216306957.

[20] S. Agostinelli, J. Allison, *et al.*, "Geant4—a simulation toolkit," *Nuclear Instruments and Methods in Physics Research Section A: Accelerators, Spectrometers, Detectors and Associated Equipment* **506** no. 3, (2003) 250–303. https://www.sciencedirect.com/science/article/pii/S0168900203013688.

[21] W. Zhang, I. Oraiqat, *et al.*, "Real-time, volumetric imaging of radiation dose delivery deep into the liver during cancer treatment," *Nature Biotechnology* **41** no. 8, (2023) 1160–1167. https://doi.org/10.1038/s41587-022-01593-8.

[22] W. Zhang, I. Oraiqat, *et al.*, "Real-time, volumetric imaging of radiation dose delivery deep into the liver during cancer treatment," *Nature Biotechnology* **41** no. 8, (Aug, 2023) 1160–1167. https://doi.org/10.1038/s41587-022-01593-8.

[23] H. Klingbeil, "Ferrite cavities," in *CERN Accelerator School: Course on RF for Accelerators*, pp. 299–317. 1, 2012. arXiv:1201.1154 [physics.acc-ph].

[24] I. Rodriguez, S. Brooks, J.-B. Lagrange, A. Letchford, C. Jolly, C. Rogers, D. Kelliher, J. Speed, J. Boehm, and S. Machida, "FFA magnet prototype for high intensity pulsed proton driver," *JACoW* **IPAC2023** (2023) TUPM032.

[25] D. P. de Boer and E. Yamakawa, Private Communication, 2024.

[26] Y. Takahoko and M.Takashima, "Measurement of betatron tunes in KURRI FFAG Main ring," FFAG WORKSHOP'09J, 2009.

[27] M. Gasior, "Base-Band Q (BBQ) Measurement with Direct Diode Detection (3D)," http://mgasior.web.cern.ch/pro/bbq/index.html.

A Summary of key events since 12-month review

Date	Event
10.01.2024	Joint ISIS/LhARA FFA meeting, https://indico.stfc.ac.uk/event/933/
24.01.2024	LhARA 3rd Peer-Group Consultation https://indico.stfc.ac.uk/event/923/
26.04.2024	ITRF 18-month review / LhARA Collaboration meeting 5 https://indico.stfc.ac.uk/event/986/
15.05.2024	10th ITRF Advisory Commmittee meeting

B Document approval

Document Approval		
Name	**Role**	**Date**
Andy Goulden	Project Manager ITRF	17$^{\text{th}}$ July 2024
Massimo Noro	Project Sponsor ITRF	17$^{\text{th}}$ July 2024
Colin Whyte	Project Manager LhARA	17$^{\text{th}}$ July 2024
Ken Long	Principle Investigator LhARA	17$^{\text{th}}$ July 2024